The Journal of Undergraduate Research in Physics

CONTENTS

VOLUME 11, NUMBER 2

MAY, 1993

Published by the Physics Department of Guilford College
for
The American Institute of Physics and The Society of Physics Students

THE JOURNAL OF UNDERGRADUATE RESEARCH IN PHYSICS

This journal is devoted to research work done by undergraduate students in physics and its related fields. It is to be a vehicle for the exchange of ideas and information by undergraduate students. Information for students wishing to submit manuscripts for possible inclusion in the Journal follows.

ELIGIBILITY

The author(s) must have performed all work reported in the paper as an undergraduate student(s). The subject matter of the paper is open to any area of pure or applied physics or physics related field.

SPONSORSHIP

Each paper must be sponsored by a full-time faculty member of the department in which the research was done. A letter from the sponsor, certifying that the work was done by the author as an undergraduate and that the sponsor is willing to be acknowledged at the end of the paper, must accompany the manuscript if it is to be considered for publication.

SUBMISSION

Two copies of the manuscript, the letter from the sponsor and a telephone number where the author can be reached should be sent to:

Dr. Rexford E. Adelberger, Editor
THE JOURNAL OF UNDERGRADUATE
RESEARCH IN PHYSICS
Physics Department
Guilford College
Greensboro, NC 27410

FORM

The manuscript should be typed, double spaced, on 8 1/2 x 11 inch sheets. Margins of about 1.5 inches should be left on the top, sides, and bottom of each page. Papers should be limited to fifteen pages of text in addition to an abstract (not to exceed 250 words) and appropriate drawings, pictures, and tables. Manuscripts may be submitted on a disk that can be read by a MacIntosh™. The files must be compatible with MacWrite™, MicroSoft Word™ or WordPerfect™. Illustrations should be in a MacDraw™ PICT format or TIFF files.

ILLUSTRATIONS

Line drawings should be made with black ink on plain white paper. Each figure or table must be on a separate sheet. Photographs must have a high gloss finish.

CAPTIONS

A caption should be provided for each illustration or table, but it should not be part of the figure. The captions should be listed together at the end of the manuscript

EQUATIONS

Equations should appear on separate lines, and may be written in black ink.

END-NOTES

End-notes should be typed, double spaced and grouped together in sequence at the end of the manuscript.

PREPARING A MANUSCRIPT

A more detailed set of instructions for authors wishing to prepare manuscripts for publication in the Journal of Undergraduate Research in Physics can be found in Volume 11 #2 which appeared in May of 1993.

SUBSCRIPTION INFORMATION

The Journal is published twice each academic year, issue # 1 appearing in October and issue # 2 in May of the next year. There are two issues per volume.

TYPE OF SUBSCRIBER	PRICE PER VOLUME
Individual	$US 5.00
Institution	$US 10.00

Foreign subscribers add $US 2.00 for surface postage, $US 10.00 for air freight.

Back issues may be purchased by sending $US 15.00 per volume to the editorial office.

To receive a subscription, send your name, address, and check made out to **The Journal of Undergraduate Research in Physics (JURP)** to the editorial office:

JURP
Physics Department
Guilford College
Greensboro, NC 27410

The **Journal of Undergraduate Research in Physics** is sent to each member of the Society of Physics Students as part of their annual dues.

MODELING OF THE ANNULAR MOAT OF THE CORONA HENG-O

Miguel B. Ruiz
Geological Research Division
Scripps Institution of Oceanography
University of California, San Diego
La Jolla, CA 92093
Received 2/12/92

ABSTRACT

We examine and model the flexural topography surrounding Heng-O. Heng-O is one of the many volcanic coronae found on the surface of Venus. Coronae are circular to elongated structures surrounded by the annular moat, which is often discontinuous. Using the high resolution altimetry acquired by the Magellan Venus Radar Mapping Mission, we have modeled the annular moat of Heng-O as a thin elastic plate subjected to a line load. We find the lithospheric thickness around Heng-O to be about 40 km. This value is greater than the 15 km elastic thickness that was calculated by assuming Venus and Earth lose heat at the same rate. The higher than expected elastic thickness in Venus implies that either the interior of Venus is cooler than the interior of the Earth, or that the rocks on Venus can withstand higher temperatures without becoming ductile.

BACKGROUND

The NASA Magellan Venus Radar Mapper spacecraft was launched on May 4, 1989 and was placed into an elliptical orbit around Venus on August 10, 1990. Magellan carries with it one 12.6 cm wavelength radar system that is shared among three different operations: side-looking synthetic aperture imaging (SAR); nadir-directed altimetry; and thermal emission radiometry. The objectives of the Magellan mission include determination of the Venusian geological structure, imaging of more than 70% of the surface of Venus at a resolution of better than 350 m and a determination of the topography of Venus at the same resolution.[1]

The radar, when operating, is either connected to a 3.7 m diameter parabolic high-gain antenna when it carries out SAR imaging, or to a smaller nadir-directed horn antenna when making altimetric observations. The parabolic antenna is also used to collect radiometry emission data. Both antennas are stationary on the orbiter's structure, so that aiming them requires moving the entire spacecraft. The radar system uses a 'burst mode' data collection plan that is sequenced among the three different modes of operation. [2]

Miguel is a senior majoring in physics with a minor in third world studies and political science. This project same out of research done during the '90-'91 school year. He is graduating in June of 1993 and plans to pursue a Ph.D. in geophysics.

In the altimeter mode, which we use, the radar system is connected to the horn antenna which emits a 1.1 ms long burst consisting of 17 pulses to the surface. The altimeter will determine the topography of Venus, but is unable to map above the northern and below the southern part, because of the orbital inclination of the Magellan. The along-track and across-track resolution varies depending upon the height of the spacecraft. Typically the altimeter surface footprint will have an along-track resolution of between 7 - 20 km and an across-track resolution between 12-30 km. [3]

The data collection geometry for the 12.6 cm radar system is shown in Figure 1. The data collection is done in a way that ensures the preservation of the Doppler signature of surface elements for later processing into high resolution (≈150m) radar images. The commands that control the data collection process are generated on Earth and then relayed to the radar sensor by the spacecraft command and data subsystem. The sensor subsystem is capable of operating at an altitude of 3500 km, sending the data to tape recorders aboard the spacecraft. The tape recorders store the data for later transmission to Earth. Mapping of the entire surface of Venus was completed in 243 days (1 Venusian day).

INTRODUCTION

We used the altimeter data (topography) set acquired by Magellan to investigate lithospheric flexure (plate bending) along the northern edge of the corona Heng-O. Coronae, first identified in Venera 15/16 (a Russian Satellite) images, are unique to Venus. They are circular to elongated structures that are surrounded by an annular

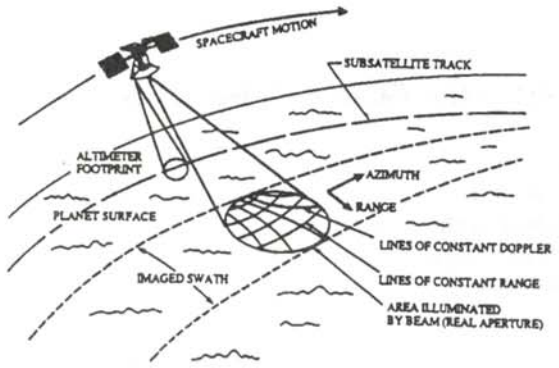

Figure 1
Geometry for SAR and altimetry data collection from an orbiting radar satellite. Range and azimuth are the across-strack and along track resolutions of the SAR.

moat which is most often discontinuous.

We modeled the annular moat as the downward flexure of the Venusian lithosphere in response to the volcanic load of the corona rim. From this modeling, we estimate the flexural parameter α, which is a measure of the width of the flexure. A short α implies a thin lithosphere while a large α implies a thick lithosphere.

For modeling purposes, we fit the individual topographic profiles to deflection curves, using the equation for deflection of a thin elastic lithospheric plate being subjected to a line load:

$$w = w_o e^{-\frac{x}{\alpha}} \left[\cos\left(\frac{x}{\alpha}\right) + \sin\left(\frac{x}{\alpha}\right) \right] + C \quad , \quad (1)$$

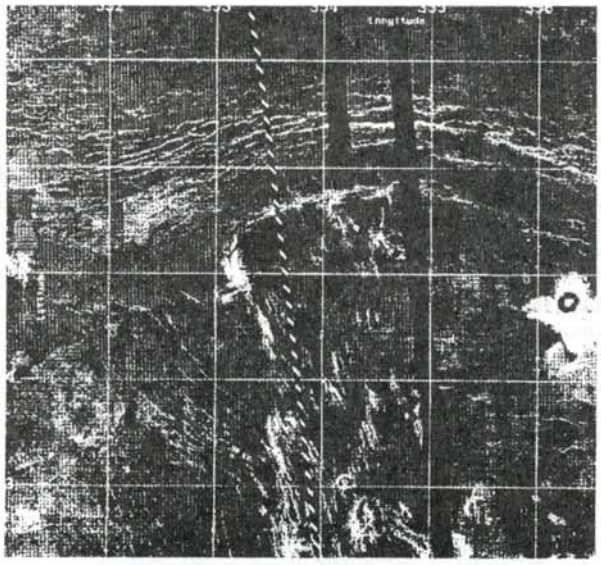

Figure 2
SAR and altimetry image of the northern margin of the corona Heng-O at 2 N, 354 E.

where C is the radius far from the flexure, w_o is the amplitude of the flexure and α is the flexural parameter, which is related to the elastic plate thickness by

$$\alpha = \left[\frac{E\, h^3}{3\, \rho_m\, g\, (1 - \nu^2)} \right]^{\frac{1}{4}} \quad , \quad (2)$$

where E is Young's modulus, h is the elastic thickness of the plate, ρ_m is the density of Venus, g the mean acceleration of gravity on Venus and ν is Poisson's ratio.[5]

DATA

We extracted altimeter profiles from the global altimeter data set to model the lithospheric flexure around Heng-O using Equation 1. The profile used for our research begins at 2°N and 354°E (the center of Heng-O) and ends at 12°N and 353°E. Figure 2 shows a SAR and altimetry image of the 850 km diameter corona of Heng-O. The profile used is marked with the striped line.

The extracted profile begins in the center of the corona, relatively featureless except for volcanoes, impact craters and small collapse features. This is followed by an abrupt rise in elevation (the rim) which extends approximately 50 km in width. The rim is immediately followed by a sudden decline in topography (1km) which is known as the trench. The trench is then followed by a mild ascension in topography (the outer rise) which gradually overshoots the mean radius of Venus (≈6051 km) and finally descends to constant topographic relief. Figure 3 shows the profile extracted from the Magellan data.

After ex`traction of the profile, we selected a data segment which includes the trench, the flexural rise and the leveling off of the topography since this part of the profile reflects the flexure of the thin elastic plate. We then fixed α and generated the function of the locations of the radius observations x_i:

$$f_i = e^{-\frac{x_i}{\alpha}} \left[\sin\left(\frac{x_i}{\alpha}\right) + \cos\left(\frac{x_i}{\alpha}\right) \right] . \quad (3)$$

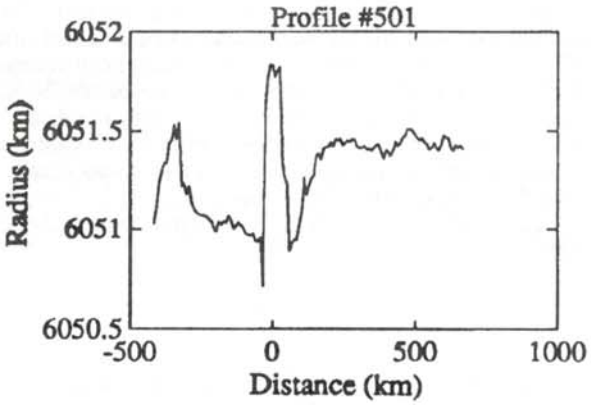

Figure 3
Profile of Heng-O. The vertical axis is the height in km from the center of the planet, the horizontal axis the distance from the rim of the corona in km.

Figure 4 shows a plot of f_i as a function of radius for our best fit.

We then plotted the observed radius as a function of f_i and fit a straight line to these points. Figure 5 shows our results for our best fit. From Equation 1, the slope of the best fit line was w_o and C the intercept, the constant radius for the flexural deformation. This line fitting procedure was repeated for varying values of h, the elastic thickness of the plate, ranging from 20 km to 60 km. The best fit of the model was for $h \approx 40$ km. A comparison between the model and the data is shown in Figure 6.

DISCUSSION AND SUMMARY

To check our modeling procedure, we extracted several profiles from the Freyja Montes region of Venus, a mountain belt located in the northern part of Venus, approximately 75°N, 33°E almost directly north of Heng-O, and compared our findings to previously published results.[6] Freyja Montes is not a corona like Heng-O, but does display evidence of lithospheric flexure, so we use it only for comparison and verification of our method. Our results for the lithospheric thickness (≈20 km) are comparable to the previous finding of 18 km. [7] This agreement in lithospheric thickness not only verifies our procedure, but it also shows that the Venera 15/16 data set agrees with the Magellan data set which we used in our study. This comparison gives us confidence in the thin plate flexure model where we have estimated an elastic thickness of the Venusian lithosphere of about 40 km.

A second estimate of elastic thickness can be made by assuming that the Earth and Venus have the same conductive heat output and that rocks on both Earth and Venus begin to flow at a temperature of 750 C. The average conducting heat flow q can be calculated by:

$$\frac{q}{k} = \frac{T_e - T_o}{h_e} \quad , \qquad (4)$$

where k is the thermal conductivity, T_e the ductile temperature, T_o the surface temperature and h_e the elastic thickness of the plate.[10] The elastic thickness determined for the Earth from Equation 4 agrees with the elastic thickness estimated by modeling the lithospheric flexure around the Hawaiian-Emperor Seamount Chain.[11].

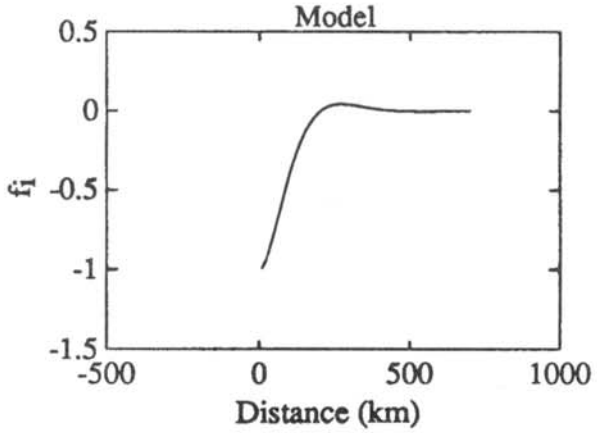

Figure 4

Results of the model shown in Equation 3 for a thickness of 40 km.

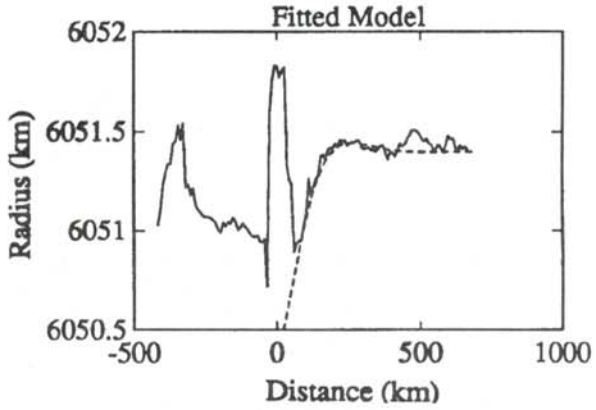

Figure 5

Fitted profile from model overlaying the topography of Heng-O for a thickness of 40 km.

Using the values found in Table 1, we calculate the elastic thickness of Venus to be ≈16 km, less that 1/2 the value of 40 km determined by the modeling of the flexure around Heng-O, but in agreement with the values found in the Freyja Montes region. There are two possible explanations for this higher than expected elastic thickness around Heng-O. The interior of Venus may be cooler than the interior of the Earth, or that the rocks on Venus can withstand higher temperatures without becoming ductile. The second explanation is not convincing, because Venera 15/16 landed on Venus and did experiments on the composition of rocks, finding no interesting properties that would make them withstand higher temperatures than rocks on Earth.

ACKNOWLEDGMENTS

The author would like to thank Dr David T. Sandwell for his valuable support throughout this research project. This work was supported in part by the NASA Geody-

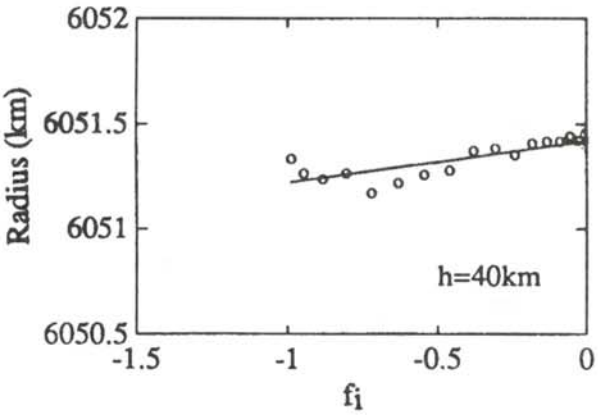

Figure 6

Least squares fit used to determine the amplitude of the flexure.

namics Program (NAGS-1226).

REFERENCES

1. G.H. Penttengill, P.G. Ford, W.T.K. Johnson, R.K. Raney, L.A. Soderblom," Magellan: Radar Performance and Data Products", Science, 252, 1992, p. 5003.
2. Ibid.
3. Ibid.
4. S.W. Squyres, D.L. Blindschaler, D.M. Janes, G. Schubert, V.L. Sharpton, E.R. Stofan, "Morphology and Evolution of Coronae and Ovoids on Venus", Magellan Conf. Abstract, 1991.
5. D.L. Turcotte, G. Schubert, Geodynamics, Applications of Continuum Physics to Geological Problems, John Wiley & Sons, Inc. 1982.
6. S.C. Solomon, J.W. Head," Lithospheric Flexure Beneath the Freyja Montes Foredeep, Venus: Constraints on Lithospheric Thermal Gradient and Heat Flow", Geophys. Res. Lett., 17, 1990, p. 9.
7. Ibid.
8. Ibid.
9. Turcotte and Shubert, op.cit.
10. A.B. Watts, "Analysis of Isostasy in the World's Oceans 1. Hawaiian-Emperor Seamount Chain", J. Geophys. Res., 83, 1978, pp. 5989-6004.
11. Solomon and Head, op.cit.

FACULTY SPONSOR

Professor David T. Sandwell
Scripps Institution of Oceanography
Geological Research Divison
University of California, San Diego
9500 Gilman Drive
La Jolla, CA 92093

Lithospheres		
	Earth	Venus
Average Conductive Heat Flow	$q_e = 90 mW/m^2$	$q_v = 0.95\ q_e$
Surface Temperature	$T_o = 0C$	$T_o = 455C$
Mechanical thickness from heat flow	$h_m = 35$ km	$h_m = 15$ km
Mechanical thickness flexure	trench 14- 72 km	static 20-74 km
Other assumptions: All heat lost by conduction; Both planets have the same thermal conductivity; The surface temperature has been constant		

Table 1
Parameters used in Equation 4. We assumed the properties for Venus except for the surface temperature.

CONSTRUCTION OF AN INEXPENSIVE TORQUE MAGNETOMETER FOR MAGNETIC THIN FILM RESEARCH

Ruediger Held
Department of Physics
Stetson University
DeLand, FL 32720
received October 21, 1992

ABSTRACT

The construction of an inexpensive torque magnetometer is described. The apparatus is made out of surplus parts and items readily available in most physics departments. The system consists of a rotating magnet, sample holder assembly, counter torque system, PID controller, laser and laser pick-up system, and a data acquisition computer. The construction and function of these components are explained in detail. The system was tested on a 10 nm Fe on $In_xGa_{1-x}As$ (x = .17) thin magnetic film. The film exhibited an unexpected uniaxial anisotropy in addition to the expected four fold symmetry.

INTRODUCTION

Torque magnetometers (TOM) can be used to investigate the properties of magnetic materials, especially magnetic thin films. TOM's are based on a sensitive torsion balance. An electromagnet is rotated around a magnetic sample. The torques induced on the magnetic sample is recorded versus the angular position of the external magnetic field of the electromagnet. Using torque magnetometry, we were able to determine various magnetic properties of a sample under investigation: magnetization; magnetic anisotropy energy; uniaxial anisotropy energy and exchange coupling of multilayer films. Many of these properties are currently not fully understood. Torque magnetometry provides a way to better understand the magnetic processes in these materials.

We tested our system on a 10 nm Fe on $In_xGa_{1-x}As$ (x = .17) magnetic thin film. The substrate on which the Fe film resides was designed to eliminate stress in the film. Usually, magnetic thin films undergo stress when they are put on a substrate, which in turn effects their magnetic properties. By trying to create a substrate that closely matches the crystalline structure of the thin film, these stresses can be minimized. The magnetic properties of the thin film than can be explored in the unstressed state.

MAIN PARTS OF THE SYSTEM

The torque magnetometer constructed was based upon a sensitive torsion balance galvanometer shown in Figure 1. The system was based on a design by Penoyter [1] and later improvements by Aubert [2]. A sample was attached to a sample holder that was located between the pole faces of a rotating electromagnet. The sample holder was connected by a rod to a coil located above the magnet between the pole faces of a stationary permanent magnet. A small mirror was mounted on top of the coil. This whole assembly was supported by a very thing gold strip. When the magnet was rotated around the sample, a torques was placed upon the sample, turning the whole assembly of holder, rod, coil and mirror. By allowing just the right amount of current to go through the coil, a counter torque can be introduced into the system, keeping to assembly always at the same orientation.

To determine the torque placed upon the sample, the mir-

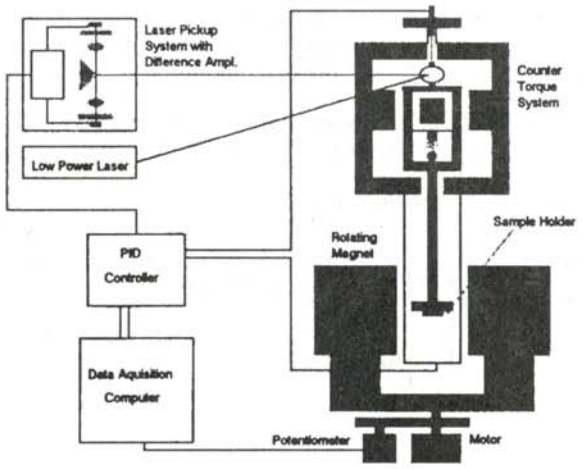

Figure 1
Overview of the torque magnetometer system.

Ruediger Held is a senior physics major at Stetson University. He has been active in research at Stetson for two years. He is planning to attend graduate school in physics when he graduates.

ror on top of the coil was used. A laser beam was directed at the mirror and reflected into a laser pick-up system. It consists of a prism that split the incoming beam into two components, both falling on separate photo resistors. Any difference in illumination of the photocells is detected and sent to a Proportional, Integral, Differential (PID) controller, whose purpose is to provide just the right amount of current to the coil to counter-balance the torque placed upon the sample. The counter-balancing current going through the coil was proportional to the torque on the coil. This current, or respective coil voltage, and the position of the magnet is detected by a data acquisition computer. Graphing the coil voltage versus the position gave us the torque acting on the sample as a function of the direction of the external field.

THE ROTATING MAGNET

We modified the pole faces of a magnet from a surplus magnetic sector mass spectrometer to supply a good homogeneous field. The pole faces had a diameter of 2.5" and were separated by 1.75". The magnet was powered by an adjustable current stabilized power supply [3] A peak field of 0.21 T was obtained with this configuration. Any electromagnet with an appropriate power supply and homogeneous field would do.

The magnet was mounted on a rotating platform, which was coupled by a step down gear box to a stepper motor. The stepper motor was driven by a controller from a kit which was modified to be stepped manually or by a computer. The same gear that was connected to the gear box of the stepper motor was connected to another gear (1:1 ratio). This gear was connected to a 10 turn 500 Ω precision potentiometer. We determined the angular position of the magnet by placing 30 VDC across the potentiometer and measuring the voltage at the center tap.

SAMPLE HOLDER ASSEMBLY AND COUNTER TORQUE SYSTEM

The center piece of the counter torque system consisted of an modified old torque galvanometer made by Leeds & Northrup Co. The torque galvanometer consists of a closed housing with a glass plate on the front. A steel rod, which can be rotated was mounted on top of the housing leading into it. A fine (.0015") gold strip was attached to this rod, supporting a mirror and coil between a permanent magnet in the housing.

A coiled gold strip was attached beneath the coil to a fixed pin on the housing. The two gold strips also function as the leads to the coil. The coil could be rotated by placing a voltage across the two gold lead leads. A bracket was mounted around the coil, supporting a fiberglass rod. The rod led through a drilled hole in the housing to the sample holder between the pole faces of the rotating magnet. An outer 1" aluminum tube was connected to the housing of the torque galvanometer. The outer tube serves to protect the sample holder from air currents as well as local temperature changes. Two leads went from the gold wires to the input of the PID controller.

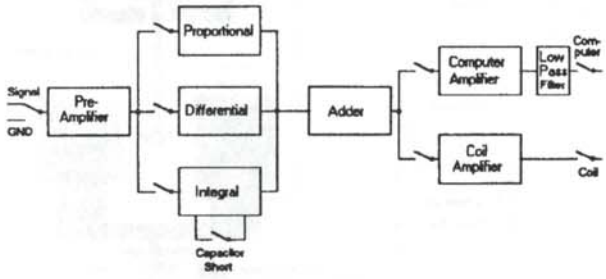

Figure 2
Schematic diagram of the PID controller.

THE LASER PICK-UP SYSTEM

The beam of a low power He-Ne laser was positioned on the mirror on top of the coil of the counter torque system. The beam was directed to the edge of a prism in the laser pick-up system. The prism split the beam into two parts, each leading through a 10 cm focusing lens and a diffusing glass slide (a microscope slide work on with sand paper) onto a photo resistor. Both photo resistors were serving as a resistor in a Wheatstone bridge connected to a difference amplifier built with a 741 operational amplifier. The output of the difference amplifier was connected to the input of the PID controller. The whole laser pick-up system was enclosed in a box with only a hole for the incoming laser beam to prevent optical noise. If the beam moves off the center of the edge of the prism, one of the arms has an increase in resistance and the other a decrease in resistance, so the difference amplifier gets a non-zero signal which then is used as the feed back signal to balance the torques

THE PID CONTROLLER AND DATA ACQUISITION UNIT

The controller's purpose was to provide the required amount of current to the coil to counter-balance the torque on the sample, keeping the laser beam always centered on the edge of the prism in the laser pick-up system. The PID controller consists of the components shown in Figure 2. A pre-amplifier received the input signal from the laser pick-up system. The output of the pre-amps goes to a linear amplifier, a differential amplifier and an integral amplifier hooked in parallel. Their outputs are added together by a gain 1 amplifier whose output goes to two linear amplifiers, one that supplied the output voltage to the coil and the other that supplied the

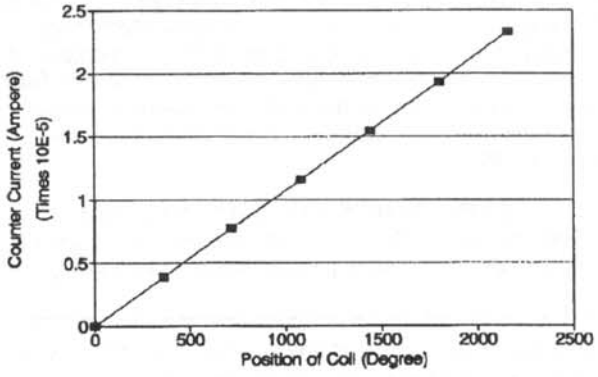

Figure 3
Calibration of the coil by plotting the counter current versus the rotation of the gold strip.

voltage to the data acquisition computer. All amplifiers used in the PID controller are appropriately wired 741 operational amplifiers.

The PID controller works as follows. When the laser pick-up system reports a voltage different from zero, the linear amplifier responds to supply a linear counter torque to the coil to correct the offset. If only the linear amplifier were used, the systems tends to oscillate about zero voltage and the laser pick-up system tends to lose the laser beam. To compensate for this, a differential amplifier responds to the the of change of any deviation from the zero point. As the oscillation tends to get bigger, the differential amplifier outputs a larger correction voltage to suppress these oscillations. The integral amplifier was used to compensate for effects that cause the laser beam to slowly float away from the center of the prism.

The PID controller has controls for the input resistance (capacitance), feedback resistance (capacitance), and zero offset for all the amplifiers. Therefore, the gain of all these components could be adjusted to optimize performance.

The data acquisition system was done by a 286 computer with an analog/digital card. [4] This card could also provide the signal for the stepper motor if we choose.

CALIBRATION

To calibrate the computer reading to torque, we had to determine the torsion constant of the straight gold strip. This was done by attaching aluminum disks to the gold strip and finding the torsional period. The torsional constant of the curled gold strip could be neglected since it was found to be much smaller than that of the straight gold strip.

The period of a torsion harmonic oscillator is:

$$T_o = 2\pi\sqrt{\frac{I}{k}}\ , \qquad (1)$$

where I is the moment of inertia and k is the torsion constant. Substituting the moment of inertial of a disk:

$$I = \frac{1}{8} m d^2, \qquad (2)$$

where d is the diameter of the disk and using Equation 1 to find k yields:

$$k = \frac{\pi^2 m d^2}{2 T_o^2}\ . \qquad (3)$$

The torque required to displace the oscillator an angle θ from equilibrium is:

$$\tau = k\,\theta\ . \qquad (4)$$

When a current i is placed through the coil, a torque:

$$\tau = c\,i \qquad (5)$$

is exerted on the system. Combining Equations 4 and 5 gives a way of determining the constant c

$$c = \frac{k\,\theta}{i}\ . \qquad (6)$$

The results of the calibration test are shown in Figure 3.

Using Ohm's law, Equation 5 becomes:

$$\tau = \frac{c}{R} V_{coil}\ . \qquad (7)$$

The voltage V, read by the computer, is just the gain of the amplifier (g) times the voltage across the coil. Equation 7 then becomes:

$$\tau = \frac{c\,g}{R} V = \alpha\, V\ . \qquad (8)$$

The calibration constant a for our apparatus was determined to be $(1.8 \pm 0.1) \times 10^{-8}$ Nm/V. Torques as small as 1×10^{-9} Nm could be measured with our apparatus. This compares favorably with results obtained by other groups [5].

DATA PRESENTATION

The system was first tested on a 10nm Fe on $In_xGa_{1-x}As$ (x = .17) thin magnetic film, supplied to us by the University of Minnesota. Data were taken by rotating the magnet around the sample 360°. Since every complete turn was symmetric around 180°, we averaged both 180° parts to reduce noise.

The total magnetic energy density for a cubic crystal can be written as: [5]

$$E = -\,\mathbf{M}\cdot\mathbf{H} + K_1(\alpha_1^2\alpha_2^2 + \alpha_2^2\alpha_3^2 + \alpha_3^2\alpha_1^2) \qquad (9)$$

where K_1 is the cubic anisotropy constant and the α_i's are the direction cosines of M relative to the cubic axes of the Fe lattice. For a thin film, the magnetization is confined to the plane of the film, so we obtain:

$$E = K_1 \cos^2\phi\ \sin^2\phi\ - MH\cos(\phi - \phi_h)\ , \qquad (10)$$

where ϕ is the angle that the magnetization makes with the [100] axis and ϕ_h is the angle that the applied field

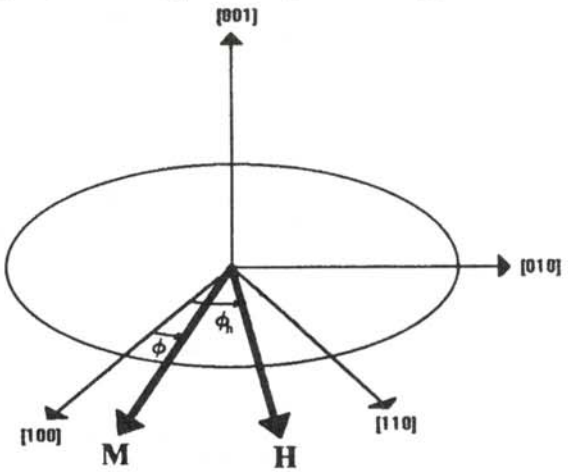

Figure 4
Diagram of the applied field H and the magnetization M with respect to the crystal axes.

makes with [100] axis as shown in Figure 4. Using some trigonometric identities, we can show that:

$$E = -\frac{K_1}{8}\cos(4\phi) + \frac{K_1}{8} - MH\cos(\phi - \phi_h)\,. \quad (11)$$

We neglect the constant term since the zero of energy is arbitrary.

For our experiment, we applied a large enough magnetic field so that **M** was always saturated along the direction of the applied field **H** ($\phi = \phi_h$). Thus, the **M°H** term is also constant and will also be neglected in the derivation that follows.

The torque per unit volume in the external field is:

$$\tau = -\frac{\partial E}{\partial \phi}\,, \quad (12)$$

This is the rotational analog of the force being minus the gradient of the potential energy. Using Equation 11 gives:

$$\tau = -\frac{K_1}{2}\sin(4\phi)\,. \quad (13)$$

This implies that the torque vs ϕ curve should be four fold symmetric and that $K_1/2$ the amplitude of the curve. However, our data shown in Figure 5, was not four fold rotation symmetric. This leads us to consider the possibility of a stress induced two fold (uniaxial) anisotropy, characterized by an anisotropy constant K_u. This term increased the energy required to align the magnetization in a direction ϕ_u relative to the [100] axis. This term is common in magnetic films grown on lattice mismatched substrates. The energy density becomes.

$$E = -\frac{K_1}{8}\cos(4\phi) + K_u\cos^2(\phi - \phi_u)\,, \quad (14)$$

and the corresponding torque per volume becomes

$$\tau = -\frac{K_1}{2}\sin(4\phi) + K_u\sin[2(\phi - \phi_u)] \quad (15)$$

Figure 5 shows typical data at a 0.2 T field. The curve was fitted using the first two coefficients of a Fast Fourier Transform (FFT) of the original data. From the Fourier coefficients and the nominal volume of the sample, assuming the 10 nm thickness is correct, we used Equation 15 to find that $K_1 = 8.54 \times 10^4$ J/m^3, Ku = 2.41×10^4 J/m^3 and $\phi_u = 47°$.

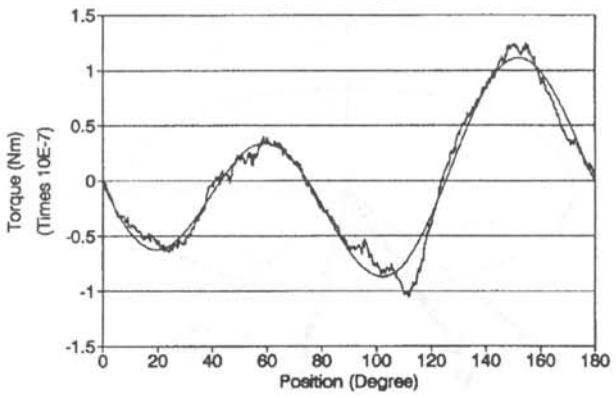

Figure 5
Torque versus angle at 0.2 T. The smooth curve is a fit to the data using 2 terms of a Fast Fourier Transform.

The value of K_1 is about a factor of 2 larger than the accepted value for bulk Fe. Typically K_1 in films decreases slightly as the thickness decreases. We attribute this discrepancy to the difficulty in accurately determining the thickness of these very thin samples. The large value of K_u relative to K_1 is also surprising, considering the idea for growing the films on a lattice matched substrate was to minimize stress induced uniaxial anisotropy. The direction of the uniaxial anisotropy, in the [110] direction ($\phi_u \approx 45°$) is consistent with results of studies of Fe grown on GaAs.

From Equation 12, one can obtain the magneto static energy from the torque curve by direct integration. Figure 6 shows the magnetic free energy for the same data.

SUMMARY

The preferred directions of magnetization can be seen in Figure 6, the magnetic free energy curve. The energy minima are the preferred directions of magnetization, or easy axes, as opposed to the peaks which are the unfavorable or hard axis of magnetization. A large magnetic field has to be applied to keep the magnetization in these hard directions. The uniaxial anisotropy breads the symmetry of the two hard directions, making one axis much harder than the other.

Fe crystals alone exhibit no uniaxial anisotropy, but a four fold symmetry with four preferred directions of magnetization (easy axes in the [100] plane). When the film is placed on a substrate, it under goes stress, which dramatically changes its magnetic properties. The Minnesota group tried to eliminate this stress by placing the film on a substrate with the same lattice characteristics as the Fe. Since we did not see the four fold symmetry, we conclude that either factors are present in thin films other than stress which influence their magnetic properties, or that the substrate and film were stressed after all.

ACKNOWLEDGMENTS

The author would like to thank Dr. Kevin Riggs for guidance through the project, as well as lab partners Steve Hewlett and Garrett Granroth for their help. The

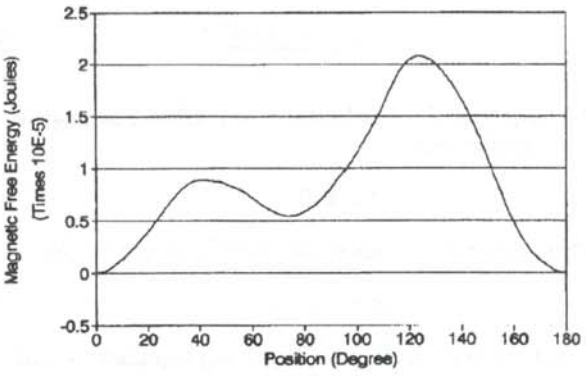

Figure 6
Magnetic free energy versus angle.

support of a Joseph H. DeFrees Award of the Research Corporation is gratefully acknowledged. The author would also like to thank Dr. Dan Dahlberg of the University of Minnesota who provided us with the thin magnetic film samples. Special thanks go to Kris Beard who did all the necessary machine shop work to make this project possible.

REFERENCES

1. R.F. Penoyer, Rev. Sci. Inst., 30, 1959, p. 711.
2. G. Aubert, J. Appl. Phys., 39, 1968, p. 504.
3. General Electric 22 PC 203 stabilized power supply.
4. IBM 286 computer with an IBM DACA analog/ digital card. The data acquisition software used was Unkel Scope by MIT, version 3.10.
5. C.M. Williams, et. al., J. Mag. Magn. Mat., 110, 1992, p. 61.

FACULTY SPONSOR

Dr. Kevin Riggs
Department of Physics
Stetson University
DeLand, FL 32720

PHOTOLUMINESCENCE ANALYSIS OF CdMnTe

Jennifer J. Dias *
Department of Physics
University of Missouri - Kansas City
Kansas City, MO 64110-2499
received August 18, 1992

ABSTRACT

Photoluminescence technique was used to determine the gap between valence and conduction bands and investigate the energy levels caused by donors and acceptors in CdMnTe. The number and nature of each transition observed was determined by analyzing the temperature and excitation power dependence of corresponding photoluminescence lines. In addition, the relationship between the percent composition of the CdMnTe crystal and the exciton energy was verified.

INTRODUCTION

Photoluminescence (PL) is the optical emission resulting from some electronic transitions stimulated by high intensity light. The region of our interest is located between the valence and first conduction band as shown in Figure 1. The intensities of all the transitions shown in Figure 1 are temperature dependent, they all decrease with increasing temperature, but the rate depends upon the type of transition. Band-to band transitions are important only near room temperature, so they will not be discussed because of the low temperatures used in this experiment. The other types of transitions dominate at low temperatures.

An exciton can be considered as a bound electron-hole pair which can move through a crystal. All excitons are unstable and ultimately recombine in a process in which the electron gets the energy of the valence band holes.[1] Energy is released in the recombination process in the form of a photon with energy

$$E_{LX} = E_G - E_X \quad , \qquad (1)$$

where E_G is the gap energy and E_X is the specific exciton energy.[2]

A free exciton may become bound by the Coulombic potentials generated within the crystal by impurities or point defects. The energy of a photon created in the recombination of the bound exciton (ABE if is an acceptor level and DBE if it is a donor level) is:

$$E_{LB} = E_G - E_X - \alpha E_{A(D)}, \qquad (2)$$

where $E_{A(D)}$ is the energy displacement of the acceptor (donor) levels from the valence (the conduction) band and α is a coefficient which depends upon the nature of the semiconductor material and impurity. The exciton transitions are very sensitive to the excitation power and sample temperature. This gives us an excellent means for identification of the various transitions.[3]

The presence of impurities allows for transitions from the conduction band to the acceptor band and from the donor band to the valence band. Such transitions are known as free-to-bound transitions. Their energies are:

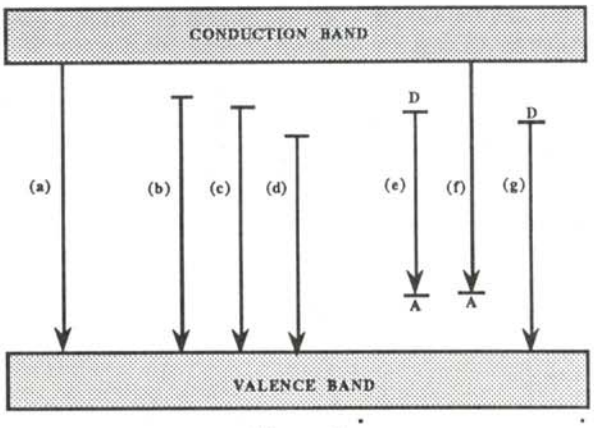

Figure 1

Some common transitions observed with photoluminescence. a) band-to-band b) free electron, c) exciton bound to donor (DBE), d) exciton bound to acceptor (ABE), e) donor-acceptor pair, f) free-to-bound (e,A), g) free-to-bound (h,D).

Jennifer Dias received her B.Sc. in physics from the University of Missouri-Kansas City in May 1992. She is currently pursuing graduate studies in physics and astronomy at Iowa State University. The research discussed in this paper was the product of an independent study during her senior year as an undergraduate. In her spare time, Jennifer enjoys dancing ballet and playing the piano.

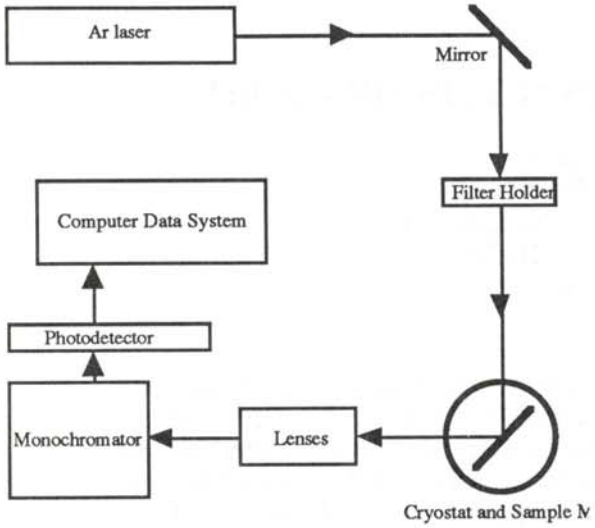

Figure 2
Experimental set up.

$$E_{FB} = E_G - E_{A(D)} + kT/2. \quad (3)$$

These transitions are also temperature dependent and can be identified by their shift to higher energies as the temperature increases.[4]

Transitions can occur between donors and acceptors. These are known as Donor-Acceptor Pair transitions (DAP). One can think of a DAP as a transition between the ground state and excited state of a molecule-like-complex formed between the donors and acceptors. This is perhaps easier than considering it a transition between a widely separated donor-acceptor pair. The energy of a DAP is given by:

$$E_{DAP} = E_G - F_C - E_A + e^2/\varepsilon r\,, \quad (4)$$

where E_A and E_D are the energies of the acceptor and donor isolated impurities. The last term is the binding energy due to pairing. [5]

Lattice vibrations often occur in the PL spectra in transitions involving three or more particles: photons, phonons and electrons. The electronic transition results in the production of a phonon whose energy is related to the energy of the no-phonon transitions. Such a phonon "replica" has an energy:

$$E_L = E_{tr} - nE_p \quad (5)$$

where E_{tr} is the energy of the principal transition and E_p is the energy of the phonon and n (an integer) is the number of phonons. E_p is characteristic of each material. These transitions can be identified at energies lower by nE_p than the principal transition. Phonon replicas can be identified by the even spaces between the non-phonon lines and the phonon lines. The phonon replica has a temperature and power dependence that follows that of the principle transition. [6]

The $Cd_{1-x}Mn_xTe$ sample that was examined in this study was produced by Dr. P. Becla at the Massachusetts Institute of Technology. The composition is stated as 40% Mn. The exciton energy obtained at 4K through the photoluminescence measurements can be used in the equation developed by D. Heiman [7] and confirmed by Yang Xia [8]:

$$E_X = 1.594 + 1.376\ X \quad (6)$$

where X is the molar fraction of Mn relative to Cd.

THE EXPERIMENT

The experimental set up is illustrated in Figure 2. The sample was mounted on a stage inside the chamber of a liquid helium cooled cryostat. The temperature in the chamber was controlled using gaseous He and a heater. The sample was illuminated with a 50mW (λ = 488.0 nm) Argon laser, focused using a conventional lens. The incident power of the laser beam was controlled using neutral density filter. The radiation emitted by the sample was focused with conventional optics on the entrance slit of a monochromator and then into a photodetector system. A computer data collection system plotted intensity versus wavelength for each measurement.

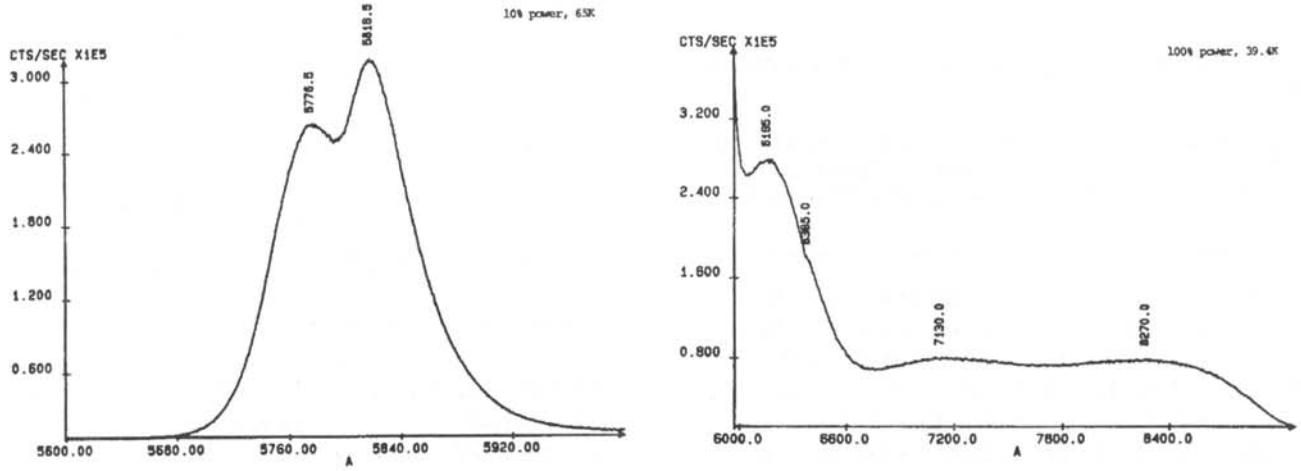

Figure 3
Transitions observed in the study sample. The two spectra are run at different laser power and at different temperatures.

In this study, the sample was subjected to variations of temperature or power. In each case, one parameter was incremented in a fairly consistent manner while the other was held constant. In the event that the signal to noise ratio became so low that the monochromator entrance slit required adjustment, all other parameters were held constant so that relative comparisons between spectra would be possible.

ANALYSIS OF RESULTS

Figure 3 shows the six transitions we measured. The numbers on the peaks are in nanometers. The band gap energy for this sample, 2.23 eV, was found using the formula: [9]

$$E_G = 1.595 + 1.592\ X \quad \text{(at 10K)} \qquad (7)$$

where X, the molar fraction of Mn, is .40.

Previous studies [10] have shown that the PL intensity is proportional to the incident power:

$$I_L \alpha\ I^{\beta}_{power}\ , \qquad (8)$$

where $\beta>1$ for exciton type transitions and $\beta<1$ for free-to-bound and donor-acceptor pair transitions. Thus, by changing the power of the laser we can identify exciton transitions. With increasing laser power, the exciton lines will increase rapidly in intensity. DAP and FB lines shift to higher energies with increasing laser power.

Figure 4 shows how the transition at 580.5nm increases in intensity with increasing power. This leads us to believe that it is probably an exciton transition. In Figure 5, a shift in the wavelength of the line at 621.0nm to 616.5nm with an increase in laser power indicated that this transition is most likely DAP.

With an increase in the temperature of the sample, the exciton line intensity should decrease rapidly. A slight red-shift occurs due to the shrinkage of the band gap. Figure 6 shows that the intensity of the lines at 577.8nm and 581.8nm decrease rapidly with increasing temperature and are, therefore, exciton lines, probably ABE and DBE. Figure 6e exhibits a slight red-shift of the remaining exciton peak. This is most likely due to band gap shrinkage. Figure 7 shows how quickly the intensity of the DAP line at 6210Å decreases at the temperature decreases.

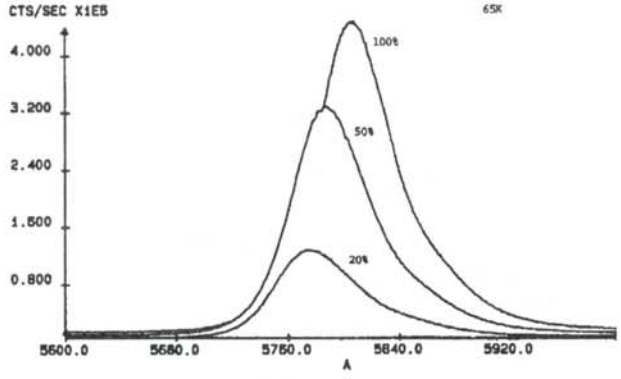

Figure 4

The 5600 Å - 6100Å region at two different power levels of the Ar laser. The increase in intensity with power indicates that this is an exiton line.

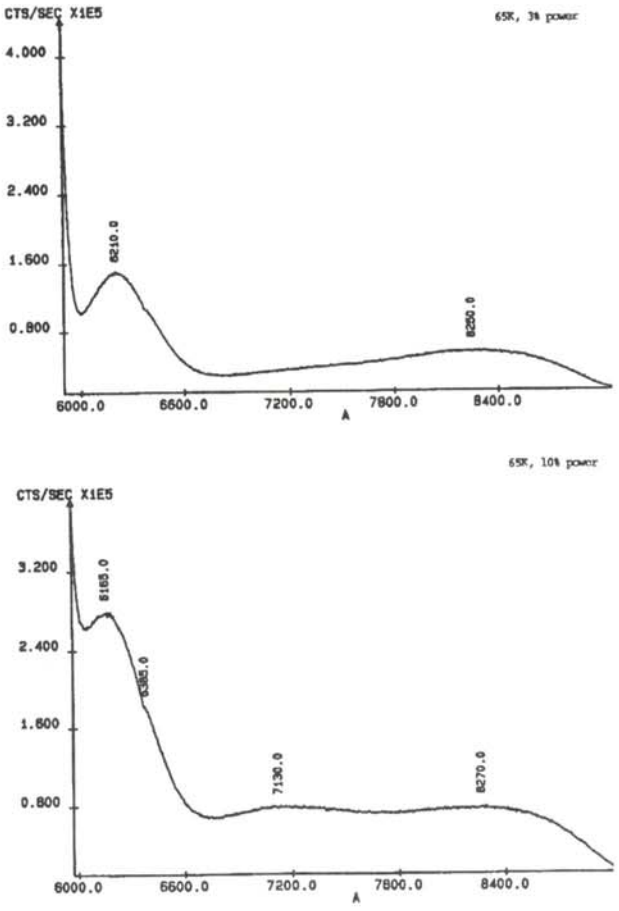

Figure 5

The 5790Å - 9100Å region at two different power settings for the argon laser. The shift of the 6219Å line to 6165Å with an increase in power indicates a likely DAP.

This leaves three transitions to identify. The transition almost obscured by the DAP line at 6308Å is most likely a phonon replica of the DAP line. It exhibits the same power and temperature dependence and is always a constant interval above the DAP line. The remaining two transitions are believed to be defect bands or possibly DAP, the data available does not allow for definitive identification. It is currently believed that defect bands arise from crystal imperfections in the form of cadmium vacancies.

Using Equation 6 and the exciton peak at 5771.5Å at 6.88K, we determined that the percentage of Mn in the sample is 40.2%. However, this number is only a good approximation, since Equation 6 was developed for a temperature of 4K. It is likely that the percent Mn is slightly higher because the exciton peak at 4K would be of slightly higher energy. This agreement between the stated and calculated values reconfirms Equation 6.

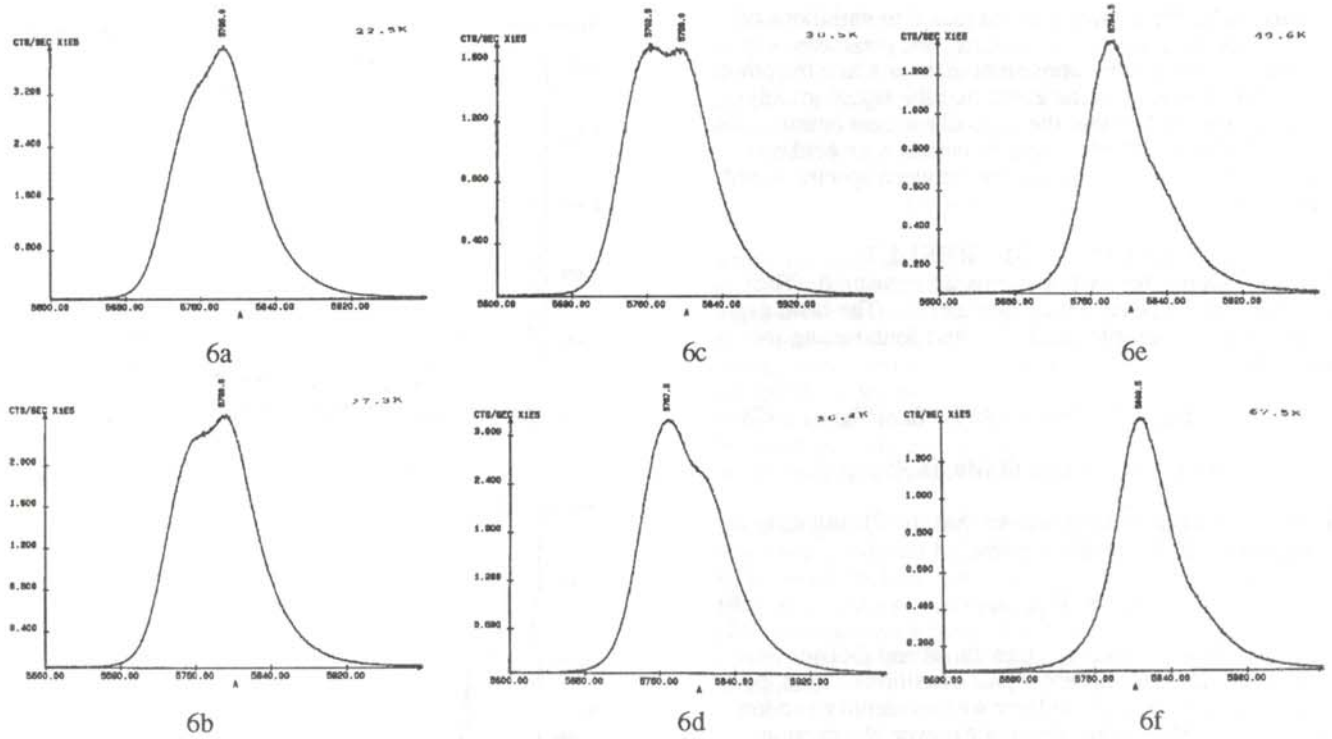

6a 6c 6e

6b 6d 6f

Figure 6

The temperature dependence of the 5600Å - 6100Å region of the photoluminescence spectrum. [a) 22.5K b)27.3 K c) 30.5K d) 36.4 K e) 49.6K f) 67.5 K\] The lines at 5778Å and 5818Å decrease rapidly with increasing temperature and are probably ABE and DBE exciton lines.

ACKNOWLEDGMENTS

The author would like to thank Dr. Jerzy M. Wrobel of the University of Missouri at Kansas City for his advice and assistance in the course of the research and preparation of this paper. The research is part of a study supported by Research Corporation Grant C-3005.

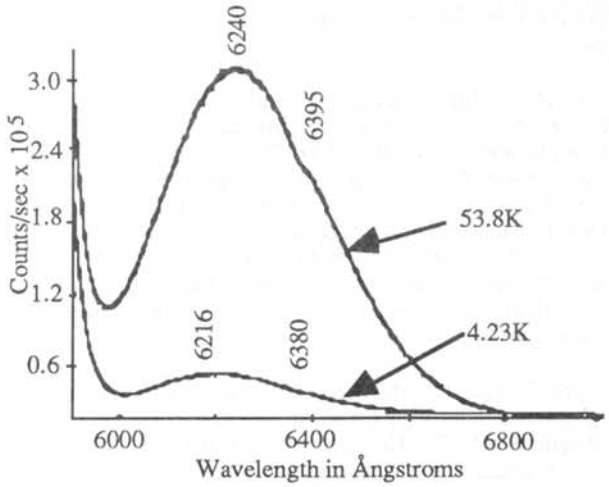

Figure 7

Temperature dependence of the 5900Å - 7000Å region of the photoluminescence spectrum.

REFERENCES

* present address of author: Department of Physics and Astronomy, Iowa State University, Ames, IA 50011.

1. C. Kittel, Introduction to Solid State Physics, 6th ed., John Wiley and Sons, Inc., New York, 1986.
2. H.B. Bebb and E.W. Williams, Semiconductors and Semimetals, Vol. 8, edited by R.K. Willardson and A.C. Beer, Academic Press, Ny, 1972, p. 302.
3. Loc. Cit., pp. 306-308.
4. Loc. Cit., pp. 309-312.
5. Loc. Cit., pp. 315-317.
6. Loc. Cit., pp. 293-297.
7. D. Heiman, P. Becla, R. Kershaw, D. Ridgley, A. Weld and R.R. Galazka, Phys. Rev. B, 34, 1986, p. 3961.
8. Y. Xia, "Low Temperature Photoluminescence Study of $Cd_{1-x}Mn_xTe$", M.Sc. Thesis, 1990, unpublished.
9. Ibid.
10. Y.R. Lee and A.K. Ramadas, Soid State Comm., 51, 1984, p. 861.

FACULTY SPONSOR

Dr. Jerzy Wröbel
Department of Physics
University of Missouri-Kansas City
1110 East 48th Street
Kansas City, MO 64110-2499

GRAPHICAL REPRESENTATION AND PREDICTION OF HALF-LIVES OF NUCLEI

Attila Báder and Tamás Kovács
Physics Department
Kossuth University
Debrecen, Egyetem Tér 1.
H-4031 Hungary
received June 1, 1992

ABSTRACT

Three dimensional systematics of radioactive nuclei are presented. The stability peninsula (the half-lives as a function of the neutron and proton number) is displayed from several views. These figures were used to work out a prediction method for the half-lives of nuclei which is based on interpolation or extrapolation of the measured values of half-lives. We tested the method by predicting some measured values. As a result, some unknown half-lives were predicted. In our work, only experimental data were used.

INTRODUCTION

So far, about three thousand nuclei have been synthesized. One of the physical characteristics of the different nuclei is the half-life. There are some theories that can be used to predict the half-life of nuclei. [1] However, one can find empirical methods that are based on experimental data only to predict them as well. An example is the work of L. Sarkadi and I. Török. [2] They plotted the half-lives of nuclei as a function of mass number. A similar diagram from our set is shown in Figure 1. These two dimensional figures were used to interpolate or extrapolate the unknown half-lives. Since then, hundreds of new nuclei have been synthesized and old measurements of half-lives have been corrected. Since the earlier work was done, computer technology has developed considerably, making it possible to display three-dimensional figures easily.

DATA

Our half-life data originated from four main sources:
a) The IAEA Nuclear Data Center, Vienna, Austria, provided us with an up to date set of half-life values, extracted from their Evaluated Nuclear Structure Data File (ENSDF). [3]
b) The IAEA also sent us a copy of the Chart of the Nuclides. [4]
c) J.K. Tuli of the National Nuclear Data Center, Brookhaven National Laboratory, USA, was so kind as to send us the latest half-life data, prepared for his booklet prior to publication.[5]
d) We searched for data in the library of the Institute of Nuclear Research of the Hungarian Academy of Sciences.

The data were prepared by plotting the half-lives of the nuclei on a logarithmic scale as a function of the neutron and proton number. The data points of nuclei which

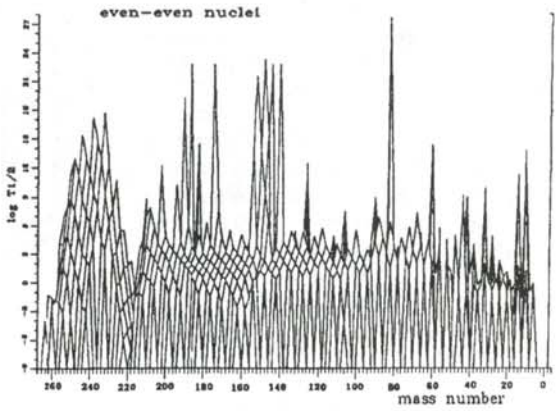

Figure 1
The half-lives of even-even nuclei as a function of the mass number. The stability peninsula is seen from the neutron deficient side.

Attila Báder and Tamás Kovács are spending their last (fifth) year at Kossuth University where they are students of physics. They were working for years in the Institute of Nuclear Research at Debrecen on different themes. They presented this work at the 1991 conference of Hungarian undergraduate student researchers. The recent interest of Attila is neural networks and that of Tamás is energy-band calculations of ion doped polymers. The hobby of Attila is orienteering sport. Tamás enjoys music in his spare time.

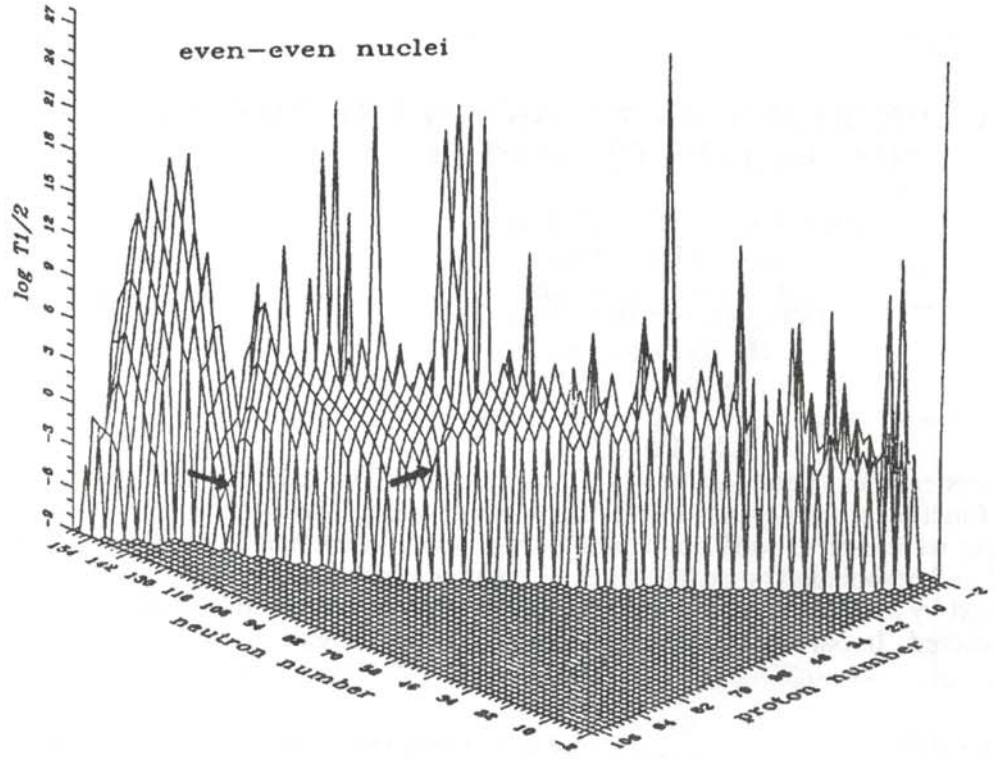

Figure 2

The half-lives of even-even nuclei as a function of the neutron and proton number. The figure shows the stability peninsula from the neutron deficient side. The arrows indicate the instability after magic numbers.

have the same proton number or same neutron number were connected with lines. The nuclei were divided into four groups according to the different types of parity of their nucleon numbers (even-even, even-odd, odd-even, odd-odd) The first term refers to the proton number and the second to the neutron number. We displayed the half-lives of different parity nuclei separately because the nucleon pair correlation effects the stability of the nuclei. This means that the half-life depends upon the type of parity.

The whole work consists of 24 diagrams, showing the stability peninsula from different views in four types of drawings. Some examples are shown in the following. Figure 1 shows the half-lives of the even-even nuclei as a function of the mass number. Figure 2 shows the half-lives of even-even nuclei as a function of the neutron and proton number. Figure 3 shows the odd-even nuclei, but only the proton lines are drawn. Figure 4 shows the even-odd nuclei with the hidden lines also displayed.

In the graphs, especially Figure 4, there is a long deep valley, stretching down the middle of the peninsula that represents the stable nuclei that are missing from our systematics. Since only 4 stable odd-odd nuclei can be found in nature, the valley mentioned before consists of 4 holes in the graphs for the odd-odd nuclei. In some places, such as those marked in Figure 3, there are holes at the edge of the peninsula if the half-life of a nuclide has not yet been measured.

Upon studying the stability peninsula in Figure 2, one can observe that at the magic proton or neutron numbers, (2, 8, 20, 50, 82, 126) the surface is not very smooth. After the magic numbers, the stability of the nuclei decrease considerably. This is most conspicuous at the proton number 82 and the neutron number 126. We explain this property of stability using the shell model of nuclei. At magic numbers, a shell is filled, which results in relatively high stability (as in the case

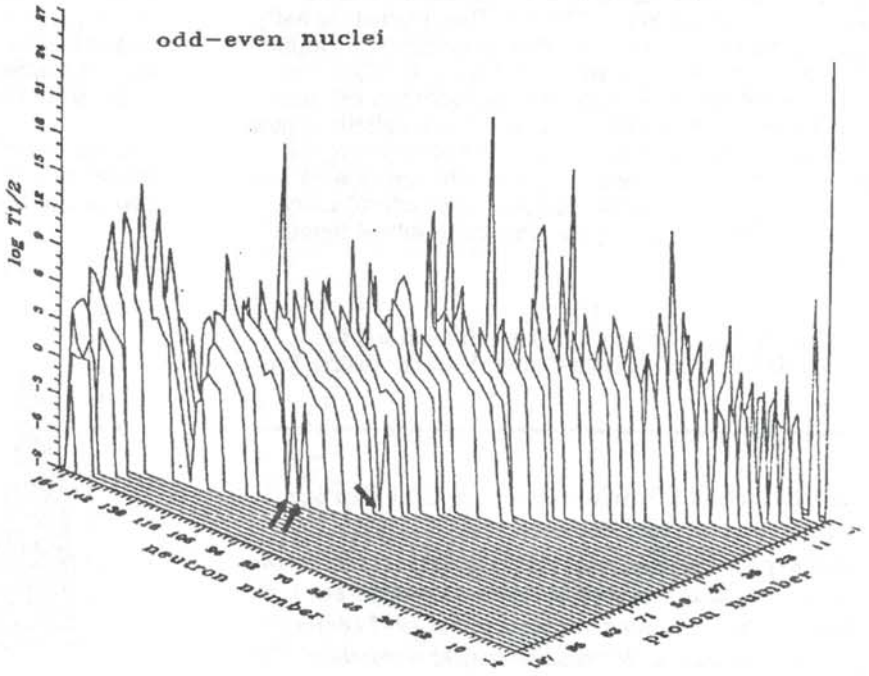

Figure 3

The half-lives of odd-even nuclei from the netron deficient side. Only the lines of constant proton number are shown. The arrows indicate the sites of not yet measured values.

of noble gases among atoms). After magic numbers, new shells begin to be filled, causing instability and roughness on the surface of the stability peninsula. This roughness makes prediction more difficult at magic numbers.

PREDICTION METHODS

We tested three different interpolation or extrapolation methods for predicting the half-lives of nuclei. In each method, the first step was to have a look at the proper figure of the stability peninsula to see whether the neighborhood of the nucleus is smooth enough. To describe the three methods, we introduce the following notation: (N,P) refers to a nucleus consisting of N neutrons and P protons and T(N,P) is the half life of this nucleus.

I. The first method is useful in the case of an (N,P) nucleus which has 6,7 or 8 neighboring nuclei (N±2,P), (N,P±2) or (N±2,P±2) with measured half-lives. In this case we can use :

$$\log T(N,P) = \frac{\sum_i [\log T(i)\ d(i)^p]}{\sum_i d(i)^p} \qquad (1)$$

where T(i) is the half-life of the neighbor and d(i) is a weighting factor which corresponds to the neighbor's distance from the (N,P) nucleus {1 in the case of (N±2,P) or (N,P±2) and 2 in the case of (N±2,P±2)}. The value of the power p should be negative, since the closer neighbors have to be taken into account with more weight. We found that the best choice for p is -3 or -4.

II. The second method is an extrapolation method. It is based on the recognition that the lines connecting those points on the surface which belong to the isotope nuclei are locally and roughly parallel:

$$\log T(N-2,P) - \log T(N,P) \approx \log T(N-2,P-2) - \log T(N,P+2) \qquad (2)$$

This equation is valid for the neutron rich side of the stability peninsula. A similar equation holds for the other side. Using these equations, we can calculate the value of T(N,P) using only the values of T(N-2), T(N-2,P+2) and T(N,P+2).

III. This third method is very similar to the second one. The lines which connect the (N,P) and the (N+2,P+2) nuclei, those which differ from each other by an alpha particle, have the properties described in the previous method, so the T(N,P) value can be predicted in a similar manner.

These three methods are independent of each other, so we can use them in parallel (if possible) to predict the value of the half-life. In this way, we are able to give a more confident prediction of the half-life.

Method	Number of Neighbors	Goodness Within a factor of 5	Goodness Within a factor of 2
I	8 nuclei	90%	62%
I	7 nuclei	89%	60%
I	6 nuclei	73%	24%
II		79%	51%
III		61%	< 20%
II - III		96%	61%

Table 1

Result of the tests of the different methods. The goodness percentage are the ratio of the tested nuclei that are within a factor of 5 or 2 of the measured values.

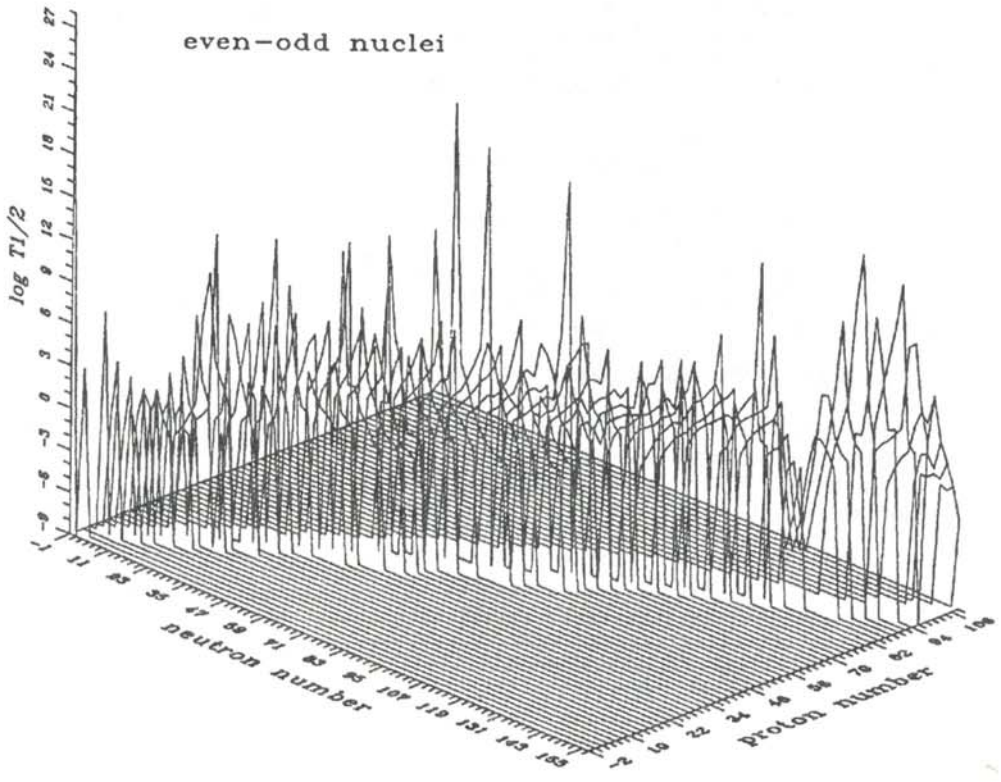

Figure 4

The half-lives of even-odd nuclei from the neutron rich side. The hidden lines are aslo shown. One can see the sites of the stable nuclei in the middle of the stability peninsula.

TEST AND RESULTS

The three methods were tested by predicting known half-life values. We chose more than a hundred nuclei for the tests. The 'Chart of the Nuclides' [4] was used to choose the nuclei. For the purposes of this paper, we considered a predicted value to be 'good' (accurate) if it was within a factor of 5 of the measured value, and to be very accurate if it was within a factor of 2. We summarize our results in Table 1. The goodness of our results is given as the percentage of all the investigated nuclei fulfilling the above conditions. The accuracy of the first two methods are satisfactory, while that of the third method can only be used in combination with the second method.

Finally, we predict some half-lives that have not yet been measured. These results can be found in Table 2. We also include previous theoretical predictions for the half lives of the nuclei.[1] In two cases, ^{67}Se and ^{93}Br, our predictions differ considerably from the previous theoretically calculated ones. We are looking forward to the experimental data.

Nucleon	Our Prediction			Theoretical
	method	halflife	goodness	Prediction
^{33}Al	I - 8nn	0.6 sec	90%	0.5 sec
^{107}Sb	I - 6nn	2 sec	73%	3.7 sec
^{53}Sc	I - 6nn	2.7 sec	73%	1.5 sec
^{106}Zr	II - III	0.2 sec	96%	0.8 sec
^{118}Ba	II - III	5 sec	96%	5 sec
^{67}Se	II - III	0.8 sec	96%	0.3 sec
^{85}Be	II - III	0.3 sec	96%	0.3 sec
^{93}Rh	II	6 sec	79%	5 sec
^{93}Br	II	30 msec	79%	0.4 sec
^{150}La	II - III	0.6 sec	96%	2 sec
^{106} Sb	II	2 sec	79%	1 sec.

Table 2

Our predictions for the half-lives of some unknown nuclei compared to the theoretical predictions of reference (1). We give the method used and its goodness according to Table 1. nn stands for 'number of neighbors'. There are two nuclei (^{67}Se and ^{93}Br) where the two estimates differ considerably.

ACKNOWLEDGMENTS

We are very grateful to the IAEA Nuclear Data Center, Vienna, for providing the latest half-life data from ENSDF and for sending a Chart of the Nuclides. We highly appreciate the kindness of J.K.Tuli for sending us his data prior to publication. Thanks are due to our consultant Dr. I. Török who has helped us during our work.

REFERENCES

1. K. Takahashi, M. Yamada and T. Kondoh, "Beta-Decay Half-Lives Calculated on the Gross Theory", Atomic Data and Nuclear Data Tables, 12, 1973, p. 101.
2. L. Sarkadi and I. Török, "Half-Life Systematics of the Radioactive Nuclides", Atomki Bull., 18, 1976, p. 609 and 19, 1977, p. 283.
3. Evaluated Nuclear Structure Data Files, International Atomic Energy Agency, 1989.
4. F. W. Walker, J.R. Parrington and F. Feiner, Chart of the Nuclides, 14th Edition, Revised April, 1988.
5. J.K. Tuli, Nuclear Wallet Cards, July, 1990.

FACULTY SPONSOR

Dr. I. Török
Institute of Nuclear Research
of the Hungarian Academy of Sciences
Debrecen, Bem tér 18/c
H-4001 Hungary

THE MAKING OF A SEMICONDUCTOR LASER

Tabatha Dolney
Physics Department
Sam Houston State University
Huntsville, TX

Fernando Ochoa
Department of Physics
University of Texas at San Antonio
San Antonio, TX
received September 7, 1992

ABSTRACT

We grew, fabricated, processed and tested a semiconductor laser which would operate at a low threshold current and have an optimum light output. A semiconductor laser is a p-n junction, similar to those found in transistors, with an active region where the recombination of electrons and holes results in the emission of photons. The laser structure chosen was an $Al_xGa_{1-x}As$ - GaAs, single quantum well, separate confinement heterostructure which emits radiation in the infrared region. The structure was grown by Metal-Organic Chemical Vapor Deposition and characterized using an electron microscope. Photolithography and metal evaporation were then used to process the laser device. A Fabry-Perot cavity was cleaved for the high reflectivity necessary to amplify the emitted light. The laser was tested by measuring the electroluminescence from the device.

BACKGROUND AND THEORY

The basic principles underlying the operation of the laser were established long before the device was successfully demonstrated. Stimulated emission and absorption were first enunciated by Albert Einstein in 1916. Theodore H. Maiman developed the first working laser in 1960. The laser used a synthetic ruby crystal as the active medium. It is believed that the first proposal for a semiconductor laser was made in an unpublished manuscript written by John von Neumann in 1953.[1] In 1962, four laboratories, working independently, reported the successful operation of the semiconductor injection laser.

The semiconductor injection laser is a p-n junction of the type found in transistors. They have sophisticated internal structures which make them perform with high efficiency. The compounds used in the the fabrication of the p-n junction must have a direct bandgap, such as those made from Group III and Group V elements, e.g., AlGaAs and GaAs. If the semiconductor has an indirect band gap, such as Si, then a phonon must be emitted in order to conserve the momentum of the electron in transition from the conduction to the valence energy band. Radiative recombination in these systems is a three-body problem, and therefore, probabilistically unfavorable. Thus, such semiconductor materials are not capable of stimulated emission. The p-type and n-type materials forming the junction must be heavily doped so that the Fermi level will lie within the conduction band of the n-type material and within the valence band of the p-type material. To create a p-type material with AlGaAs, a Group II element such as Zn is used as a dopant to form an excess of holes. For an n-type material, a Group IV element such as Sn is used to create an excess of electrons.

Current can be carried by both negatively charged conduc-

Fernando is a senior majoring in physics at the University of Texas at San Antonio. He is presently assisting a professor in research of laser efficiency for laser triggered nuclear fusion. After graduation from UTSA, he plans to pursue a Ph.D. in high energy physics.

The fall after the completion of this laser project, Tabatha graduated from Sam Houston State University with a B.Sc. in physics. She has altered her course from that of physics research to the path of science education. She is presently striving for her teacher's certification from Texas A&M University

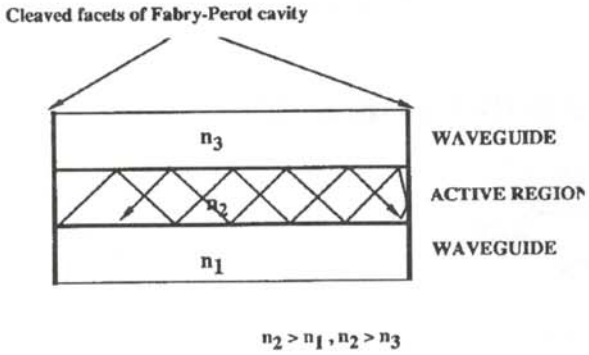

Figure 1

Ray trajectories of the guided wave in the Fabry-Perot cavity. The cleaved facets reflect radiation back and forth, while the waveguide layers confine the radiation to the active region.

tion electrons and 'holes' that carry a positive charge. The movement of the holes is caused by the electrons jumping between vacancies. Thus, the holes will appear to move in the opposite direction of the free electrons. Applying a forward bias to the p-n junction provides the 'active region' at the junction, with a large supply of electrons in the conduction band and holes in the valence band. This forms a type of population inversion necessary for laser action. In the active region under forward bias, the free electrons are captured by the holes in the valence band in a process called recombination. This movement of electrons from higher to lower energy levels causes the spontaneous emission of energy in the form of photons of energy hv, approximately equal to that of the gap between the conduction and valence bands.

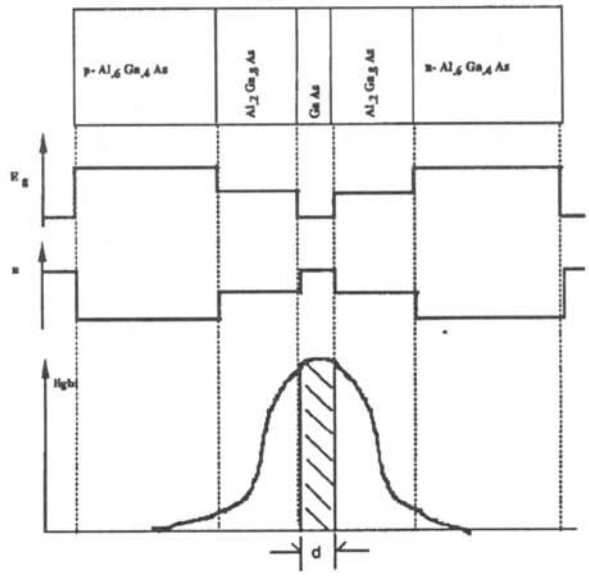

Figure 2

Schematic representation of the energy band gap, refractive index and light intensity for the cladding, wav eguide and active regions of a separate confinement heterostructure laser.

This energy difference, called the bandgap energy E_g, is characteristic of the material.

To make a useful laser, a material must have reflective surfaces to reflect the photons back into the material so that more electrons in the higher energy state can jump to the lower energy state by stimulated emission. Cleaved facets from a highly reflective Fabry-Perot cavity reflect the photons back and forth through the pumped material causing even more stimulated emission. At this point, the injected current must also be at the threshold value to provide the necessary amount of electron-hole pairs for stimulated emission to occur.

The various layers of the semiconductor laser, which can be as small as 10 nm., were grown by Metal-Organic Chemical Vapor Deposition (MOCVD). The metal-organics used have high vapor pressure and can be transported to the reaction area by passing a carrier gas through the liquid source or over the solid sources. The metal-organic and hydride compounds are mixed in the vapor phase and are pyrolyzed in flowing H_2 gas in a low-pressure reactor. The prolysis reactions occur at the substrate, which sits on a susceptor heated to temperatures between 600C and 800C and rotated at 800 rpm for uniform growth. MOCVD has been found to have great advantages, such as high purity and monolayer control, although the chemistry of the gas phase and surface catatlyzed reactions are still not completely understood. [2] This type of device could be used in applications such as optical communications and computer manufacturing because of its high efficiency and light output.

DESIGN OF THE LASER

Optical Confinement

A laser must have a reflective cavity in which most of the radiation is confined. The cleaved facets of a Fabry-Perot cavity reflect radiation back and forth within the active region as shown in Figure 1. The desired effect is the optimum ratio of light intensity coming from within the active region to the total amount of light both outside and inside the active region of the laser schematically shown in Figure 2. This ratio, called the confinement factor Γ, is given for a simple three-layer waveguide by

$$\Gamma = 1 - \exp\{-C\,\Delta n\, d\} \qquad (1)$$

where C is a constant, Δn is the change in refractive index between the cladding and the waveguide layers and d is the thickness of the confined region. The larger the value of d, the larger the value of Γ and the more powerful the laser.

Electrical Confinement

Another desired feature of a laser is a low threshold current density. This can be achieved by growing the active region to a thickness on the order of the carrier deBroglie wavelength:

$$\lambda = h/p \qquad (2)$$

where h is Planck's constant and p is the momentum.[3] At this thickness, the active region can be considered as a finite square well with energy levels that are similar to the 'particle in a box' solutions. Recombination of elec-

tron-hole pairs follows the quantum mechanics selection rule $\Delta l = 0$ as it occurs between two well-defined density of states. [3] Photon scattering in a quantum-well structure, caused by higher energy electrons cascading to a lower density of state, can lead to laser operation at an energy less than E_g, the bandgap energy. Therefore, confinement of the electron-hole recombination to a quantum-well active region results in a low threshold current. By defining a small area of the laser structure using thin strip metal contacts through which the current will be pumped, a low threshold current density can be achieved.

STRUCTURE OF THE DEVICE

We chose to construct a $Al_xGa_{1-x}As$-GaAs single quantum well, separate confinement heterostructure (SQW SCH) as shown in Figure 3. The quantum well was a thin layer (≈20 nm) of GaAs which produced a wavelength of ≈850 nm, corresponding to a slight increase in energy relative to the bandgap energy of 1.43 eV. [4] The layers above and below the quantum well serve as optical waveguides that confine the radiation to the active region. The refractive indices of the layers around the active region must be less than the refractive index of the quantum well layer for optical confinement to occur. [4] Since there is a direct relationship between the concentration of aluminum and the refractive index of AlGaAs [5], the confinement factor and the refractive indices were used to determine the aluminum concentration (see Figure 3) of the waveguides and the cladding layers. Another significant layer was the AlGaAs 'ramp' where the concentration of the aluminum varied from 0.20 to 0.60. We knew from previous growth data that the ramped layer reduces the resistance in the n-type doped layers. The 'buffer' layers absorb any contaminants during the growth of the crystal. The thin quantum well and the high Γ from the separate confinement layers should make a laser with a low threshold current density.

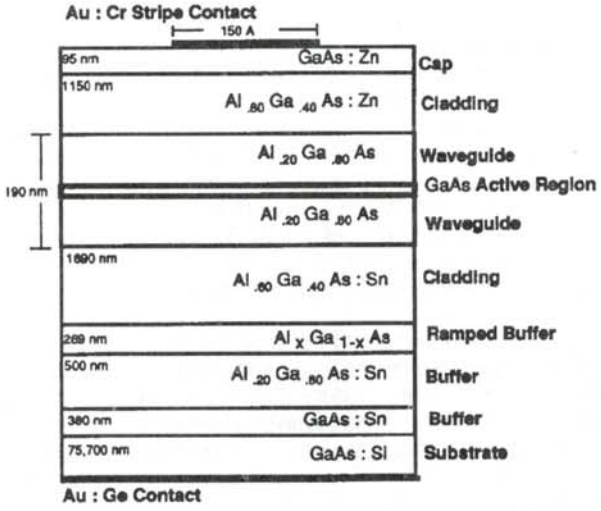

Figure 3

SQW SCH laser structure schematic. The diagram shows the thickness taken from the SEM photograph in Figure 4, the materials and the functions of each layer of the laser structure.

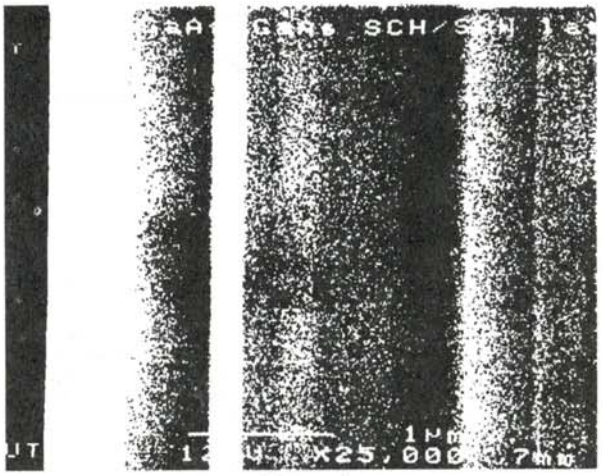

Figure 4

Micrograph of the laser structure taken by a scanning electron microscope. This was used to measure the layer thicknesses of the grown structure.

The growth times for each layer were determined using known growth rates for the MOCVD reactor. The 'buffer' layers were grown before the active layer to absorb any contaminants, such as oxygen, that remained in the chamber from previous growths. The total time for crystal growth was 77.3 minutes.

CHARACTERIZATION OF THE LASER

After the laser structure was grown, tests were performed to characterize the material and confirm the desired layers and compositions.

Scanning Electron Microscope

A scanning electron microscope (SEM) micrograph, shown in Figure 4, of the grown structure was used to measure the thickness of the layers. The thickness of the layers were measured on the photograph and then divided by 25,000, the magnification of the SEM. The calculated layer thickness using the known growth rates for the MOCVD reactor and the measured thicknesses differed by about 5%. The layers were not well defined in the SEM micrograph due to the poor contrast, so the measurements were not precise, yet suitable for this project.

X-ray Diffraction

The composition of the $Al_xGa_{1-x}As$ layers was determined by X-ray diffraction. The distance between the AlAs (x=1) peak and the GaAs (x=0) substrate peak is a known value of 0.1042 degrees. As the concentration, x, of Al decreases, the angle $\Delta\Theta$ between the two peaks changes. The concentration x is:

$$x = \Delta\Theta \,/\, 0.1042. \qquad (3)$$

X-ray diffraction spectra were taken twice on the same sample, but in two different areas, to assess the uniformity of the growth.

The X-ray source was a Cu $K_{\alpha 1}$ with a wavelength of 1.5406Å. The lattice structure of AlGaAs and GaAs is zincblende, which is two face centered cubic lattices off-

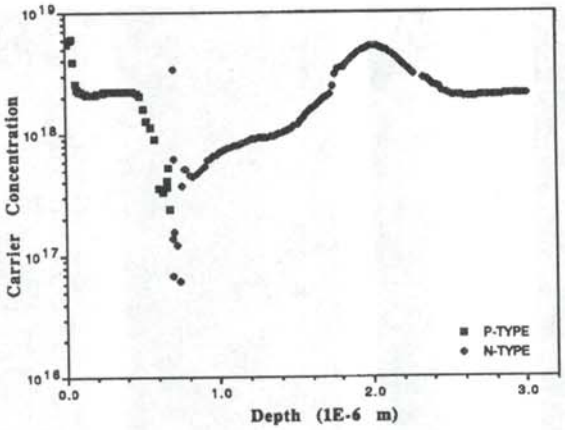

Figure 5

Carrier concentration versus depth. These results from the electrochemical etch show the change of carrier concentration through out the depth of the laser material. The low points indicate the active region, while the high points indicated the highly doped cladding layers.

set by 1/4, 1/4, 1/4. The Miller indices of the reflecting planes were [400]. The peaks from $Al_{.60}Ga_{.40}As$ and $Al_{.20}Ga_{.80}As$ showed concentrations of 0.57 and 0.23 in the first spectrum and 0.56 and 0.22 in the second spectrum. These results were satisfactory as the composition of aluminum in these layers provide the necessary refractive indices for the laser structure.

Carrier Profiling

A third method of characterization used was carrier profiling, using an electrochemical profiler. It chemically drills a hole into the laser material and measures the p-type and n-type carrier concentrations. The results showed the concentration of electrons or holes as a function of the depth of the laser structure. This test confirmed the level of doping that we desired in each layer.

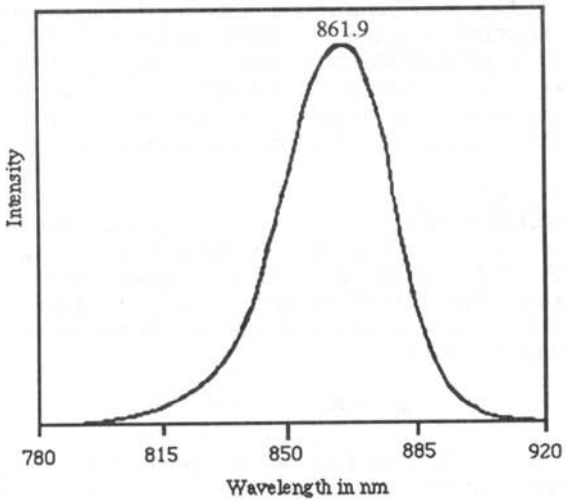

Figure 6

Results of electroluminescence measurements, showing the structure acting as a Light Emitting Diode (LED) below the operating threshold current.

Figure 5 shows the levels of p-type carriers at the top of the structure and then how the levels decrease in the wave guide and the active region and how the carriers change to n-type through the bottom half of the device. The concentration of carriers show that the layers formed a suitable p-n junction for electrically pumping our quantum well active region.

FABRICATION AND PROCESSING

The fabrication included metalization, photolithography and other steps to bring the laser material to the appropriate size and shape. The first step involved 'lapping' away part of the initial GaAs substrate in order to get the material thin enough to cleave the Fabry-Perot edges. A thin substrate also reduced the electrical resistance. The original thickness of the material was about 400 μm with the epitaxial layers adding about 3.8 μm. The thickness after lapping needed to be about 100 μm.

A metal contact was then evaporated on the substrate. A layer of 21.6 nm of Ge and a layer of 121.3 nm of Au was evaporated onto the substrate layer and then put through rapid thermal annealing for 30 seconds at about 400 C to combine the two elements into an alloy.

The cap of the laser was then metalized. We used photolithography to lay 150 μm strips of Cr and Au over the top of the material. The thin strips reduce the area of the material that will exhibit laser action, resulting in a lower threshold current density. The metalization provided resistive contact to the laser material which is necessary for efficient controlled injection of current.

The final step in the fabrication of the device was to cleave the reflective Fabry-Perot edges. This resulted in bars of semiconductor lasers about 500μm. long. We tested a laser that had an electrical contact area of 150μm x 180μm.

TESTING THE DEVICE

The electroluminescence spectrum was measured to test the structure's ability to function as a laser. Two such spectra are shown in Figures 6 and 7. A constant current was injected into the laser structure and a spectrum was acquired of relative intensity of emitted photons versus the wavelength of the photon. This was done at different currents. Figure 6 shows a smooth bell shaped curve at λ = 862 nm at a current of 23.8mA. This is due to spontaneous emission. This is the type of spectrum that one would expect from a light emitting diode.

At an increased current of 238mA, the curve at λ = 862nm began to sharpen, indicating a slight amount of stimulated emission. Figure 7 shows the spectrum at a current of 381mA. The spectrum shows stimulated emission with a sharp peak at 856 nm and several peaks at oscillating modes. These wavelengths are in the infrared region. The results of the spectra show that the processed device performed as a laser.

Figure 8 shows our results for measuring the intensity of the emitted photons as a function of the injected current. The bend in the curve shows the region where spontaneous emission was overcome by the stimulated emission. The threshold current is the point where the extrapolated

straight line of the stimulated emission line crosses the axis. This low threshold current of 180mA is the amount of current needed to create the necessary population inversion of electrons and holes for laser action to occur. Our threshold current density of 0.667 kA/cm^2 compares with those obtained for similar laser structures that have been fabricated by other groups.

ACKNOWLEDGMENTS

This project was performed at the Science and Technology Center for the Synthesis, Growth and Analysis of Electronic Materials at the University of Texas at Austin under the auspices of the Summer Program for Education and Research (SPEAR). The authors would like to thank Dr. Russell Dupuis and Kirk Fertitta for their advice and direction in this project. Thanks also go to Chris Pinzone, Jim Neff, C.V. Ramachandran, Rabiul Islam, Imran Iqbal and Zhe Huang for their technical support which aided in the completion of this project. This project was supported by the Science and Technology Center Program of the National Science Foundation under grant #CHE-8920120

REFERENCES

1. R.D. Dupuis, "An Introduction to the Development of the Semiconductor Laser", IEE Hournal of Quantum Electronics, QE-23, 6, June 1987, pp. 651-657.
2. R.D. Dupuis, "Metalorganic Chemical Vapor Deposition of III-V Semiconductors", Science, 226, 9, Nov. 1984, pp. 623-629.
3. S.M. Sze, Physics of Semiconductor Devices, 2nd Edition, Wiley-Interscience, New York, 1981.

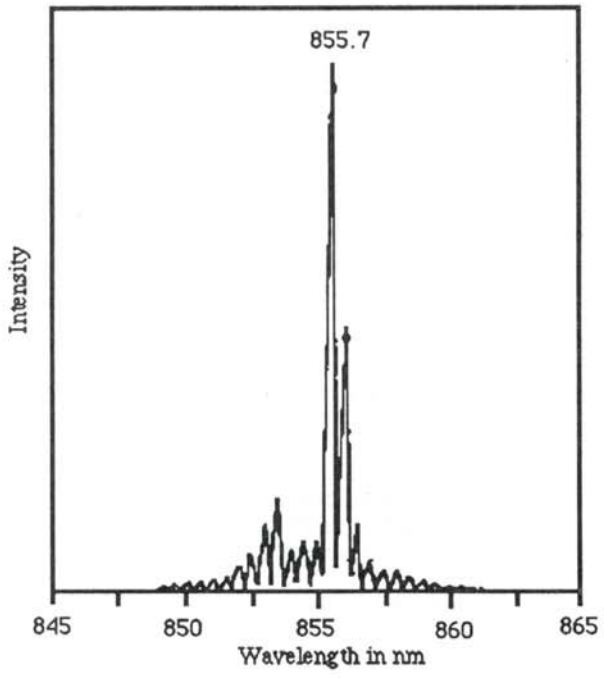

Figure 7

Results of electroluminescence measurements of the output of our laser showing the structure lasing at or above the threshold current.

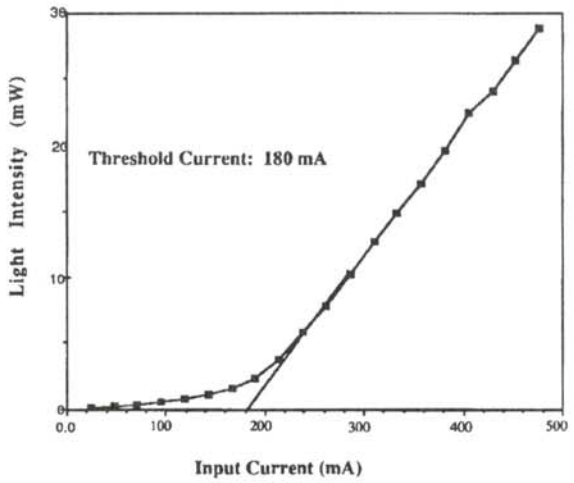

Figure 8

A plot of the output light intensity versus input current for our AlGaAs-GaAs SWQ SCH laser. The threshold current for the laser device is 180 mA.

4. B. Streetman, Solid State Electronic Devices, Prentice-Hall, New York, 1990.
5. V. Swaminathan and A.T. Macrander, Materials Aspects of GaAs and InP Based Structures, Prentice-Hall, New Jersey, 1991.

FACULTY SPONSOR

Dr. Russell D. Dupuis
Judson S. Swearingen Regents Chair in Engineering
Department of Electrical and Computer Engineering
The University of Texas at Austin
Engineering Science Building 433B
Austin TX 78712-1084

COEFFICIENT OF LIFT FOR A SPINNING BASEBALL: AERODYNAMICS OF A CURVE BALL.

Dan J. Beideck *
Physics Department
Pomona College
Claremont, CA 91711
received September 10, 1992

ABSTRACT

The coefficient of lift for a spinning baseball was measured as a function of Reynold's number. The data obtained give insight into the curve ball and allow more precise calculations of the trajectory of baseballs pitched with spin. Some sample trajectories were calculated using the data obtained along with that reported in the literature.

INTRODUCTION

The term curve ball in the broad sense covers a range of pitches from those with side-spin (axis of rotation perpendicular to the ground), to those with top-spin (axis of rotation parallel to the ground). In practice, nearly all curve balls have components of both top-spin and side-spin with an associated drop and sideways deflection respectively. The axis of rotation generally becomes closer to horizontal as the skill level of the pitcher increases. Batters typically claim that a well pitched curve ball initially follows a trajectory similar to that of a fast ball, but suddenly drops as it crosses home plate. "Dropping off the table" is an expression sometimes used to describe this motion. In this paper, the spin of the curve ball will be idealized to be solely top-spin and the associated deflection to be downward.

The deflection of a spinning sphere moving through a fluid, such as a baseball moving through air, has been commonly referred to as the "Magnus effect". The effect was named for Magnus after Lord Raleigh attributed it to him, but it was Robins who first demonstrated the existence of a deflecting force when a spinning sphere moves through the air. [1] This paper presents measurements made of this force on a baseball and goes on to incorporate the data in some simple trajectory calculations.

TRANSITION TO TURBULENCE?

There are two major aerodynamic forces acting on a spinning baseball. The first of these is drag. It is customary in aerodynamics to present dependent and independent variables in dimensionless units. The dimensionless unit for drag is the coefficient of drag,

$$C_d = - 2 F_d / (\rho A V^2) \quad , \qquad (1)$$

where F_d is the drag force (opposite in direction to the motion of the ball), ρ is the fluid density, A is the cross-sectional area of the ball and V is the velocity of the ball through the fluid (air).

The second major aerodynamic force of interest is the lift, or drop if the direction is downward. The dimensionless unit associated with lift is the coefficient of lift,

$$C_l = - 2 F_l /(\rho A V^2) , \qquad (2)$$

where F_l is the (negative) lift force (perpendicular to the direction of motion of the ball). An additional dimensionless unit, called the Reynold's number is also important:

$$\Re_e = V d / \nu \quad , \qquad (3)$$

where ν is the kinematic viscosity of the fluid and d is the diameter of the ball.

The amount of curve for a pitch is characterized better by the coefficient of lift, C_l, than by the lift force, F_l. As a pitched baseball moves a short distance d through the air, it experiences a negative lift that deflects the ball downward a distance s. It is approximately true that

$$s \approx a t^2 / 2 \qquad (4)$$

where a is the acceleration produced by the negative lift in time t. The lift force is then:

$$F = 2 m s / t^2 \qquad (5)$$

and from Equation 2,

The author received a B.A. from Pomona College in 1987. The present work was primarily done as his senior thesis. He is currently at the University of Toledo where he is a full-time research technician and a part-time graduate student.

Fluid density ρ	1.15 kg/m^3
Kinematic viscosity ν	1.61×10^{-5} m^2/sec
Wind Speed	4±2 m/sec
diameter of ball	7.32×10^{-2} m
Cross-sectional area	4.21×10^{-3} m^2

Table 1
Atmospheric and geometric data used in this experiment.

$$C_l = -\frac{4\,m\,s}{\rho\,A\,V^2\,t^2}\ , \qquad (6)$$

where m is the mass of the ball. Since V = d/t,

$$C_l = -\frac{4\,m\,s}{\rho\,A\,d^2}\ . \qquad (7)$$

Rearranging equation 7, we find:

$$s = -\left[\frac{\rho\,A\,d^2}{4\,m}\right] C_l\ . \qquad (8)$$

The part in the brackets is a constant for our purposes. Therefore, the amount of deflection is equal to a constant times the coefficient of lift and is independent of the velocity of the ball and the time of flight. On the other hand, the lift force, F_l, alone does not give the deflection

$$s = F_l\ t^2/2m \qquad (9)$$

since the time that the force is applied is critical. Therefore, it is easier to intuitively determine the deflection from the coefficient of lift than it is from the lift force

At some critical Reynold's number, the air at the surface of the ball (the boundary layer) becomes turbulent and the coefficient of drag decreases rapidly for a small increase in Reynold's number. This is called the 'drag crisis'. It seems reasonable that a similar effect involving the coefficient of lift, a 'lift crisis', might also be observed. The critical Reynold's number for the drag crisis for a smooth sphere was measured to be 3.7×10^5 (81 m/sec or 182 mph for a baseball) [2] The roughness of the surface effects the critical Reynold's number. [3] Figure 1 shows the results for two roughness parameters. The critical Reynold's number decreases as the roughness parameter, k/d (where k is the average height of roughness of the sphere), increases.

Some claim that a curve ball breaks at a nearly constant rate.[4,5,6] They believe that the drag crisis for a baseball occurs at speeds greater than those typical for the curve ball and that the coefficients of lift and drag are at most weak functions of Reynold's number. This theory predicts a trajectory of a curve ball to have essentially constant curvature and that any sudden or dramatic break that batters claim to see is an optical illusion resulting from the batter's nearly head-on view of the pitch.

Frohlich has proposed a theory which would account for a real, dramatic change in the trajectory of a curve ball near the end of its flight.[7] The height of a seam on a baseball is 0.5 mm., resulting in a roughness parameter of about 7.0×10^{-3}. This corresponds to a critical Reynold's number near 0.8×10^5 (17.6 m/sec or 39 mph). Frohlich also noted that another measurement of the coefficient of drag equal to 0.29 at a Reynold's number of 2.08×10^5 gives a critical Reynold's number close to 0.8×10^5. [8] If this is true, the curve ball is normally thrown at speeds greater than the onset of the drag crisis. He suggests that if a curve ball were thrown so that it is in the transition phase associated with the drag crisis, it would slow due to drag on the way to home plate. As the Reynold's number decreases, the drag and lift forces increase and a non-constant rate of curvature would result. Frohlich created a computer program to test the extent of this effect. He calculated the trajectory of thrown balls with different roughness parameters and a fixed initial velocity vector. His results show that the height of a pitch as it crosses home plate is dependent upon what part of the drag regime the ball is pitched.

This experiment attempts to better determine the trajectory of a curve ball by measuring the coefficient of lift as a function of Reynold's number. By doing this, it may be possible to see if there exists a turbulent transition in this region and if this transition might cause a non-constant rate of break of a curve ball.

THE EXPERIMENT

The wind tunnel available at Pomona College does not provide a sufficiently high velocity for measuring curve balls. Instead, the necessary instrumentation was designed and attached to the hood of a truck. A baseball was extended a short distance in front of the vehicle and the truck was then driven on a dry lake bed at the desired velocities (or Reynold's numbers).

The apparatus for this experiment is shown in Figure 2. A baseball was mounted on a shaft by drilling a hole into the ball and attaching a short threaded rod. The mounting shaft was connected to a DC motor. Plexiglas was used to shield the motor and mounting shaft from the wind. The motor was calibrated using a strobe light. The rotation rate was determined with a frequency counter that was connected to the output of the strobe. The procedure was repeated many times with difference voltages applied to the DC motor. There was a linear relationship between the applied voltage and the rate of rotation.

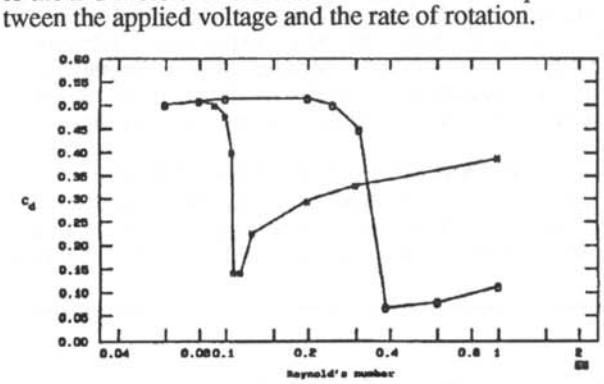

Figure 1
Drag Coefficient C_d vs Reynold's number for a sphere [2,3]. The open points are for a smooth sphere and the stars for a roughness parameter of 5×10^{-3}.

The motor assembly was attached to a second shaft and could rotate only along the axis of this shaft The shaft was attached to the motor assembly slightly above the center of gravity. This created a natural restoring torque due to gravity that was proportional to the angular displacement of the motor assembly from its static equilibrium position with the baseball on top. When the truck was moving and the ball spinning, a sideways torque on the assembly resulted due to the Magnus effect. The assembly came to equilibrium at some angular displacement where the torque caused by the lift force on the ball canceled out the torque caused by gravity. The resulting angular displacement was measured by a scale and pointer attached to the shaft. The scale was calibrated in the lab by applying a series of known torques to the motor assembly and recording the corresponding angular displacements.

The data were taken in one afternoon. Table 1 shows the atmospheric conditions and ball geometry. The rotation rate of the ball was set at 1400 rpm. The truck was driven directly into the wind and brought up to speed such that the total wind velocity was 20 m/s (45 mph). The velocity was incremented in 2.2 m/s (5 mph) intervals until a velocity of 38 m/s (85 mph) was reached. This covered the range of curve ball speeds quoted in the literature. [9,10] The angular displacement of the ball and motor assembly was recorded for each speed. The truck was returned to the same starting position and similar runs were made for rotation rates of 1600 rpm, 1800 rpm and 2000 rpm. These rotation rates span the range quoted in the literature for curve balls. [8,10]

After these data were recorded for a seam orientation where all four seams met the wind each rotation, the procedure was repeated for a second orientation where just two seams per rotation met the wind. The results for one orientation are shown in Figure 3. The results for the other seam orientation are similar.

TRAJECTORY CALCULATIONS

The data collected was used to determine the trajectory of a curve ball. The trajectories were calculated using a PASCAL program. The initial conditions: initial height 2.5 m.;initial angle above the horizontal plane of 3°;and an initial velocity of 28 m/sec (63 mph), were chosen to be as realistic as possible. A least squares fit was used on the 1800 rpm data to determine the negative lift force as a function of Reynold's number.

The program calculated the trajectory of a curve ball in

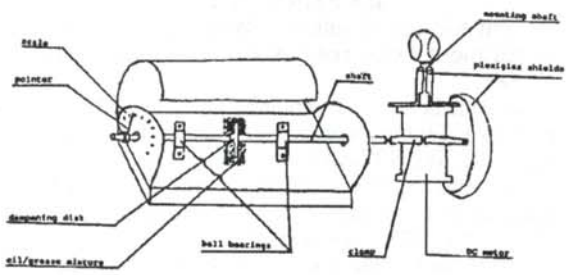

Figure 2
Experimental apparatus.

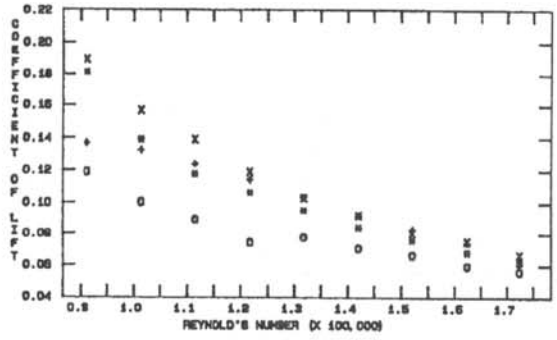

Figure 3
*Measured coefficient of lift versus Reynold's number. o - 1400 rpm, * - 1600 rpm, + - 1800 rpm, x - 2000 rpm.*

the following way. Every .2ms of flight time, the forces due to gravity, drag and lift were determined and the new position of the ball and its velocity vector were calculated. This continued until the total pitch distance in the horizontal direction was equal to 18.445 m (60 ft, 6 in.), the distance between the pitching rubber and home plate. It is true that the pitcher actually releases the ball a meter or so on the home plate side of the pitching rubber, but it is normal for the batter to stand at the back end of the batters box, also about a meter behind the plate. Therefore, the pitch distance used should be approximately correct. Step sizes smaller than .2 ms. were tried, but showed no significant differences in the calculated final height of the ball.

The drag force on the ball was calculated from a couple of different sources. The first was from data collected by Hollenberg[11] for a non-spinning baseball with an orientation angle of 42°, typical for the various angles he measured. The second was from Achenbach[3] for a roughness parameter of 5×10^{-3}. Achenbach's data were used in a couple of ways: the first in a straight forward manner or unshifted; the other way was to shift the curve so that the minimum of the coefficient of drag, shown in Figure 1, occurred at the initial velocity of 28 m/s. This was justifiable because the roughness parameter for a baseball is near 5×10^{-3}, but probably not exactly that value. For a sphere with a slightly smaller roughness parameter, the basic shape of the coefficient of drag versus Reynold's number plot remains the same, but is shifted to the right. The roughness of a baseball may be such that the coefficient of drag's minimum occurs for the Reynold's number corresponding to 28 m/s, or more likely, for a velocity somewhere near that value. A good pitcher may be able to determine by trial and error what velocity to release the ball such that the coefficient of drag is initially at a minimum. Either way, the shift was used to try to determine what is the maximum effect with a coefficient of dray of the "Achenbach type" by nominally setting the minimum of the coefficient of drag to the Reynold's number corresponding to 28 m/s.

The effect of the non-constant coefficient of lift was determined by making two separate trajectory calculations

C_l	C_d	final height (m)
zero	zero	1.332
constant(Beideck)	constant(Hollenberg)	0.733
constant(Beideck)	Hollenberg	0.728
Beideck	Hollenberg	0.706
Beideck	constant(Hollenberg)	0.712
constant(Beideck)	constant(Achenbach)	0.928
constant(Beideck)	Achenbach	0.930
Beideck	Achenbach	0.923
Beideck	constant(Achenbach)	0.921
constant(Beideck)	constant(shifted Achenbach)	0.969
constant(Beideck)	shifted Achenbach	0.860
Beideck	shifted Achenbach	0.846
Beideck	constant(shifted Achenbach)	0.964

Table 2

Final calculated height of a baseball pitched with an initial height of 2.5 m., initial velocity of 28 m/sec, a 3° inclination above the horizontal and a rotation rate of 1800 rpm. The values of C_l and C_d used are from the author indicated.

for the given drag data. One trajectory was determined using a constant coefficient of lift for the entire pitch. The coefficient of lift was set to the value appropriate for the initial velocity of 28 m/s. A second trajectory was calculated that allowed the coefficient of lift to change as the velocity of the ball changed. The effect of a non-constant coefficient of lift was the difference between the final height of the two trajectories. For completeness, two additional trajectories were calculated, this time with the drag coefficient held constant rather than a function of the Reynold's number. The results of these calculations are shown in Table 2.

INTERPRETATION OF DATA

Figure 3 shows a coefficient of lift that decreases as the Reynold's number increases. As such, the coefficient of lift would increase as a pitched baseball progresses towards home plate and is slowed down due to drag. This would cause the ball to curve more towards the end of the pitch. The size of this effect is the difference in the final height of a pitch with non-constant coefficient of lift versus one with a constant coefficient. The height difference from the trajectory calculations (see Table 2) ranged from 2.2 cm using Hollenberg's data [11] to 0.7 cm using Achenbach's unshifted data [3]. The height difference for the shifted Achenbach data was 1.4 cm. The difference due to a non-constant lift coefficient were not overwhelming, but are significant when compared to the baseball bad radius of less than 3.5 cm.

The height differential calculated here between constant and non-constant drag coefficients for the various types of data varied a great deal, from tenths of centimeters to 11.8 cm. for the shifted Achenbach data. This is potentially a bigger factor in producing an unexpected curve than the coefficient of lift has shown to be. Direct measurements of the coefficient of drag for a spinning baseball would be helpful in calculating trajectories, since it is not know how good the data of Hollenberg and Achenbach are for describing the motion of spinning baseballs.

A still better approximation of the curve ball trajectory may be necessary if the coefficient of lift or drag is a function of the orientation of the seam. Some have suggested that precession of the ball's orientation to the wind may be responsible for the sudden break. [4,10,11] If a pitcher could control the pitch such that the ball precessed to the orientation where the coefficient of lift was at its maximum just before crossing the plate, the ball would be subject to a non-constant rate of curvature. However, our data did not show a noticeable difference in the coefficient of lift for the two seam orientations used. This may be because this effect is not large and the measurement errors of this experiment were too high to detect it. Vibrations from the road and some uncertainty in the wind velocity were the major contributors of error. The errors were also too large to determine if the coefficient of lift is proportional to the wind velocity or to the wind velocity squared. There are conflicting data on this point.[6]

It is worthy of note that the physicist tends to measure the drop of the curve ball differently that a batter measures it. A physicist measures the drop as the difference between the vertical height of a curve ball and the vertical height of a ball affected only by gravity. However, there is no pitch in existence that is affected by gravity only. The batter measures the drop of the curve ball as the difference in vertical height between the curve ball and the fast ball, a larger drop than the physicist measures. The magnitude of the mean rate of rotation for a fast ball is near that for a curve ball, 1600 rpm compared to 1800 rpm. The measured rise, compared to the 'gravity only pitch', caused by the back spin on the fast ball, ranged from 9 to 82 cm. [10] Acknowledgment of the difference in ways of measurement should bring the physicist and the baseball player closer to agreement on the curve ball.

ACKNOWLEDGMENTS

The author would like to extend special thanks to Walter Ogier who made several key contributions to this experiment, including the 'screw ball' idea of taking this experiment 'on the road'. Frank Nilon, Glenn Flohr, as well as the physics departments at Pomona College and the University of Toledo also made contributions for which I am grateful.

REFERENCES

* Current address of author: Physics and Astronomy Department, University of Toledo, Toledo, OH 43606.

1. H.M. Barkla and L.J. Auchterlonie, "The Magnus or Robins Effect on Rotating Spheres", J. Fluid Mech. 47, 1971, pp. 437-447.
2. E. Achenbach, "Experiments on the Flow Past Spheres at Very High Reynold's Numbers", J. Fluid Mech., 54, 1972, pp. 565-575.
3. E. Achenbach, "The Effects of Surface Roughness and Tunnel Blockage on the Flow Past Spheres", J. Fluid Mech., 65, 1974, pp. 113-125.
4. J.F. Drury, Jr., "The Hell It Don't Curve!", The

Amer. Mercury, 1956, pp. 101-106.
5. W.J. Allman, "Pitching Rainbows: the Untold Physics of the Curve Ball", Science 82, 3, 1982, pp. 32-38.
6. R.G. Watts and R. Ferrer, "The Lateral Force on a Spinning Sphere: Aerodynamics of a Curve Ball", Am. J. Phys., 55, 1971, pp. 40-44.
7. C. Frohlich, "Aerodynamic Drag Crisis and its Possible Effect on the Flight of Baseballs", Amer. J. Phys., 52, 1984, pp. 325-334.
8. L.J. Briggs, "Effect of Spin and Speed on the Lateral Deflection (Curve) of a Baseball; and the Magnus Effect for Smooth Spheres", Amer. J. Phys., 27, 1959, pp. 589-596.
9. A.T. Slater-Hammel and E.H. Andres, "Velocity Measurement of Fast Balls and Curve Balls", Res. Q., 23, 1952, pp. 95-97.
10. C. Selin, "An Analysis of the Aerodynamics of Pitched Baseballs", Res, Q., 30, 1959, pp. 232-240.
11. J.W. Hollenberg, "Secrets of the Knuckleball", The Bent, 77, 1986, pp. 26-30.
12. F.L. Verwiebe, "Does a Baseball Curve?", Amer. J. Phys. 10, 1942, pp. 119-120.

FACULTY SPONSOR

Professor Walter T. Ogier
Department of Physics and Astronomy
Pomona College
Claremont, CA 91711

ON PREPARING A MANUSCRIPT FOR PUBLICATION

Rexford E. Adelberger, Editor

Perhaps the most important thing for you to keep in mind when you write a manuscript which you intend to submit for publication to the Journal of Undergraduate Research in Physics is that the audience that will be reading the paper are junior or senior physics majors. They are knowledgeable about physics, but unlike you, they have not spent as much time trying to understand the specific work which is being reported in your paper. They also can read English well and expect the paper to be written by a colleague, not a robot or an 'all-knowing' computer. There is a big difference between the comments you write in the margin of your lab notebook or what you might write in a technical brief and what you should present in a paper for publication in a scientific journal.

There is a difference between a Journal article and keeping a journal. Your laboratory data book should be the journal of what you did. It contains all the data, what you did (even if it was an attempt that turned out to be wrong), as well as comments as to what you were thinking at that time. The Journal article is an discussion of how you would do the research without excursions along blind alleys and hours spent collecting data that were not consistent. The reader should not necessarily be able to completely reproduce the work from the Journal article, but the reader should be able to understand the physics of what was done.

How a person uses Journal articles to find out about new ideas in physics is often done in the following way. A computerized search using key words in abstracts is done to see what work has been done in the area of interest. If the abstract seems to be about the question the reader has in mind, the body of the paper is tracked down and read. If the reader then wants to find out the finer details of how to reproduce the experiment or to see how some fine point of a derivation was done, the author is contacted for a personal in-depth conversation about the more subtle details.

The general style of writing that should be followed when preparing a manuscript for publication in the Journal is different from what you would submit to your English literature professor as a critique of some other work. The narrative is intended to do three things: 1) set the background necessary so that the reader can appreciate and understand the physics being reported in the paper; 2) discuss the details of what you did and the implications of your work; 3) lead the reader through the work in such a way that they must come to the same concluding points that you did.

When finished with your paper, the reader should not have to go back and try to decide for themselves what you did. Your narrative should lead them through your work in an unambiguous manner, telling them what to see and understand in what you did. The interpretation of the data or calculations should be done by the writer, not the reader. The interpretation of your results is the most important part of the paper.

You should take care to make sure that the material is presented in a concise logical way. You should make sure that your sentences do not have too many dependent clauses. Overly complicated sentences make the logic of an argument difficult to follow. You should choose a paragraph structure which focuses the attention of the reader on the development of the ideas.

A format which often achieves these aims is suggested below:

ABSTRACT

An abstract is a self contained paragraph that concisely explains what you did and presents any interesting results you found. The abstract is often published separately from the body of the paper, so you cannot assume that the reader of the abstract also has a copy of the rest of the paper. You cannot refer to figures or data that is only presented in the body of the paper. Abstracts are used in computerized literature searches, so all key words that describe the paper should be included in the abstract.

INTRODUCTION

This is the section that sets the background for the important part of the paper. It is not just an abbreviated review of what you are going to discuss in detail later.

This section of the narrative should present the necessary theoretical and experimental background such that a knowledgeable colleague, who might not be expert in the field, will be able to understand the data presentation and discussion. If you are going to use a particular theoretical model to extract some formation from your data, this model should be discussed in the introduction.

Where appropriate, the information should be referenced using end-notes. When presenting background information, you can guide the reader to a detailed description of a particular item with the statement such as: "*A more detailed discussion of laminar flow can be found elsewhere*[1]". If you know where there is a good discussion of some item, you don't have to repeat it, just guide the

reader to the piece.

How one proceeds from this point depends upon whether the paper is about a theoretical study or is a report on an experiment. I will first suggest a format for papers about experimental investigations and then one that describes a theoretical derivation.

Experimental Investigations

THE EXPERIMENT

This section guides the reader through the techniques and apparatus used to generate the data. Schematic diagrams of equipment and circuits are often easier to understand than prose descriptions. A statement such as "*A diagram of the circuit used to measure the stopping potential is shown in Figure 6*" is better than a long elegant set of words. It is not necessary to describe in words what is shown in a diagram unless you feel that there is a very special part which should be pointed out to the reader. If special experimental techniques were developed as part of this work, they should be discussed here.

You should also be careful to separate the discussion of the equipment used to measure something from your results. This section should not include data presentations or discussions of error analysis.

DATA PRESENTATION AND INTERPRETATION OF RESULTS

This is the most important section of the paper. The data (a plural noun) are the truths of your work. This section should lead the reader through the data and how errors were measured or assigned. The numerical data values are presented in tables and figures, each with its own caption, eg. *"The results of the conductivity measurements are shown in Table 3"*. It is difficult to follow narratives where the numerical results are included as part of the narrative. Raw, unanalyzed data should not be presented in the paper. All figures and tables should be referred to by their number.

Any figure or table that is not discussed in the narrative should be eliminated. Items which are not discussed have no place in a paper. A well written data presentation results in a reader who reaches the same conclusion as the author about the experiment.

A Theoretical Study

THE MODEL

This part should consist of a theoretical development of the constructs used to model the physical system under investigation. Formulae should be on separate lines and numbered consecutively. The letters or symbols used in the equations should be identified in the narrative, eg. *The potential can be approximated as:*

$$W \approx Z - \sigma(\rho) \qquad (1)$$

where Z is the number of protons and σ is the screening constant that is dependent on the charge density ρ of the inner electrons of the K and L shells.

If you wish to use this formula at a later time in the narrative, you refer to it by its number, eg. *"The straight line fit shown in Figure 3 means that we can use Equation 1 to extract a value of..."*

CALCULATIONS

This section presents a summary and discussion of the numerical results calculated from the model. These results should be presented in tables or graphs, each with their own caption. A table or graph which is not discussed in the narrative should be eliminated. Data that are not interpreted by the writer have no place in a paper. One should take care to reference numerical results that are used in the calculations and come from previous work done by others .

The following sections and comments pertain to both types of papers.

CONCLUSIONS

It is indeed rare that one can come to clear and meaningful conclusions in one paper. I do not know of many papers where this section should be included. What you might do is include a summary of your work.

SUMMARY

This section would include a review of all important results. Comparisons (in terms of standard deviations) of your results with those found elsewhere should be done here. This section might also include suggestions for further research that could be done on this topic.

REFERENCES

All references, numbered in order from beginning to end of the paper, are collected together at the end of the paper. You should be aware of the following format:

If the reference is a text-

1) A.J. Smith and Q.C.S. Smythe, Electromagnetic Theory, Addison Wesley, New York, 1962, p. 168.

If the reference is a journal-

2) J. Botswain, Journal of Important Results, 92, 1968, pp. 122-127.

If the reference is unpublished-

3) R.J. Ralson, private communication.

ACKNOWLEDGMENTS

This short section should acknowledge the help received (that is not referenced in the previous section) from others. This is where you would give credit to a lab partner or someone in the machine shop who helped you build a piece of equipment.

The following is a set of suggestions that will make your paper easier to understand

Figures or Tables

Tables and figures are placed by the layout editors at the corners of the page to make the format attractive and easy to read. It might happen that a figure is not on the same page as the discussion of the figure. Consequently, each table or figure should be numbered and have a caption which explains the figure. Readers often scan papers by looking at the figures and data tables before they read the narrative of the work. You should take care to put enough information in the caption of a figure or table so that the reader can get some feeling for the meaning of the data presentation. All lines shown on graphs should be identified, eg. *"The dashed line is drawn to guide the eye"* or *"The solid line is a fit to the data using the Ising model"*

An example of a graph of a set of data is shown in Figure 1. You should notice that the graph is sized by the range of data points. The bottom left point does not have to be the point (0,0). A graph with all the data points clustered in one small corner and lots of white space does not help the reader get a felling of the dependence of your data. Error bars are shown with the data points and all lines drawn on the graph are identified. A figure or table that is not discussed in the narrative part of the report serves no purpose and should eliminated.

You should be careful that the figures you present are not too busy. If you put too much information on a single figure, it becomes difficult for the reader to pick out the important parts. The paper should bring the reader to an understanding of what you did rather than to introduce a game of hide-and-seek.

Any experimentally measured numbers used in tables. such as shown in Table 1, should include an uncertainty. You should use scientific notation when presenting numbers, e.g. $(7.34 \pm .03) \times 10^7$ eV. You should take care to have the correct number of significant digits in your results. Just because the computer prints out 6 digits does not mean that they are significant. You should use the MKS system of units.

A few general comments on style

It is often helpful to make a flow chart of your paper be-

State	Experimental eV	Theoretical eV
3S	5.15±.01	5.13
4S	1.89±.02	1.93
3P	2.96±.02	3.02

Table 1

Energy states found in the numerical search. The accepted values for these states are also listed.

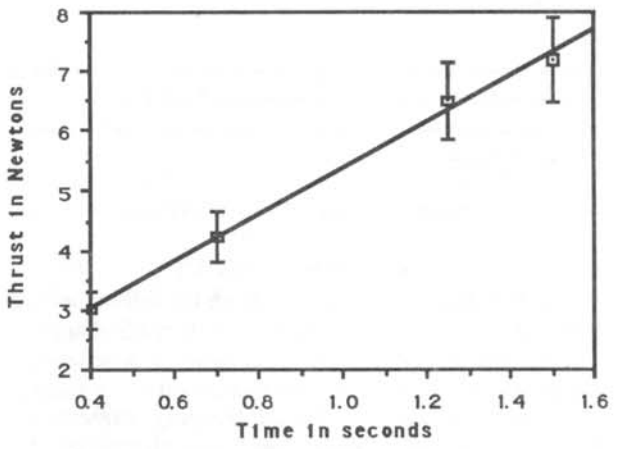

Figure 1

A graph of the measured thrust of a D-2 model rocket engine as a function of time. The line drawn is the least squares fit straight line to the data.

fore you write it. In this way, you can be sure that the logical development of your presentation does not resemble two octopuses fighting, but is linear.

One generally writes the report in the past tense. You already did the experiment. You also should use the the third person neuter case. Even though you might have done the work by yourself, you use "we". eg. *"We calculated the transition probability for..."*

It is often confusing when you begin sentences with conjunctions. Make sure that each sentence is a clear positive statement rather than an apology.

There are a few words or phrases you should be careful about using:

Fact - this is a legal word. I am not sure what it means in physics.

Proof or prove - These words are meaningful in mathematics, but I am not sure you can prove something in physics, especially experimental physics.

The purpose of this experiment is... - Often, for example, it is necessary to do the experiment to complete the requirements for your degree. You do not need to discuss the purposes of the experiment.

One can easily show that... - You should not try to intimidate the reader. What if the reader finds this difficult to show. Remember that the reader of your paper is a senior in college!

It is obvious that... or *One clearly can see....* - Such statements only intimidate the reader that does not find your work trivial. What is obvious to someone who has spent a lot of time thinking about something may not be obvious to the reader of your paper. All this will do is encourage the reader to stop reading your paper.

The Journal of Undergraduate Research in Physics

The **Journal of Undergraduate Research in Physics** is the journal of Sigma Pi Sigma and the Society of Physics Students. It is published by the Physics Department of Guilford College, Greensboro NC 27410. Inquiries about the journal should be sent to the editorial office.

The Journal of Undergraduate Research in Physics

Editorial Office -
The Journal of Undergraduate Research in Physics
Physics Department
Guilford College
Greensboro, NC 27410
919-316-2279 (voice)
919-316-2951 (FAX)

Editor -

Dr. Rexford E. Adelberger
Professor of Physics
Department of Physics
Guilford College
Greensboro, NC 27410
ADELBERGERRE@RASCAL.GUILFORD.EDU

The Society of Physics Students

National Office -
Dr. Donald Kirwin, Executive Director
Dr. Edwin Goldin, Associate Director
Society of Physics Students
American Institute of Physics
1825 Connecticut Avenue, N.W.
Suite 213
Washington, DC 20009
202-232-6688

President of the Society -
Dr. Jean Kirsch
Department of Physics
University of Michigan

President of Sigma Pi Sigma -
Dr. Reuben James
Department of Physics
SUNY College at Oneonta